Explicit Non-Linear Finite Element Analysis with Fluid Structure Coupling of a High Velocity Impact

by

Jonathan Edward Homesley

A thesis submitted to the Graduate Faculty of
Auburn University
in partial fulfillment of the
requirements for the Degree of
Master of Science

Auburn, Alabama
August 6, 2011

Approved by

Winfred A. Foster, Jr., Chair, Professor of Aerospace Engineering
Gilbert L. Crouse, Associate Professor of Aerospace Engineering
Robert S. Gross, Associate Professor of Aerospace Engineering

Abstract

A computational investigation was undertaken to study the pressure wave generated from a high velocity, multi-material penetrator impacting a compartmented cylindrical container. Variations of the penetrator material stacking order are studied to evaluate the efficiency of delivering energy to the target. The relevant application of this research, some previous work done in high velocity impact dynamics, a comparison of the different penetrator configurations, and the overall results of the analysis are discussed.

Acknowledgments

The author would like to thank the members of the advisory committee for their guidance throughout this work. Special thanks go to Dr. Winfred Foster. Without his continual advice, support, and guidance this work could not have been accomplished. The author would also like to thank his parents, Dennis and Redonda Homesley, his sister, Rachael Waddle, his brother, Nathan Homesley, and all of his friends and family for the love and encouragement they have given along the way.

Table of Contents

List of Figures

List of Tables

Nomenclature

A – Static Yield Stress
B – Hardening Parameter
C – Strain Rate Parameter
cm – Centimeter
C_P – Specific Heat
E – Modulus of Elasticity
EPS0 – Reference Strain Rate
G – Shear Modulus
in – Inch(es)
K – Bulk Modulus
lb – Pound-Force
m – Temperature Exponent
mph – Miles per Hour
MPS – Maximum Plastic Strain
m/s – Meters per Second
n – Hardening Exponent
PMIN – Minimum Spallation Pressure
psi – Pound-Force per Square Inch
sec – Second(s)
TMELT – Melt Temperature
TROOM – Room Temperature
U – Wave Propagation Velocity
v = Poisson's ratio
Y_0 – Static Yield Strength
ρ – Density
ρ_0 – Reference Density
σ – Stress
σ_{HEL} - Hugoniot Elastic Limit
σ_{yield} – Yield Stress

Chapter 1: Introduction

1.1 The Objective

The goal of the analysis is to lend understanding to situations encountered in certain military applications, particularly kinetic energy, penetrator systems for penetrating armored vehicles. To accomplish this goal an explicit non-linear finite element analysis was done to determine not only the amount of energy transferred to a compartmented cylindrical container (target) impacted by a high velocity penetrator, but also to model the resulting pressure wave transmitted through the target. The penetrating projectile is made of three equal mass rods. The three rods are each made of a different metallic material encased in a polycarbonate shell. The metallic materials used are aluminum, steel, and tungsten. More details concerning the target and penetrator dimensions, material properties, and initial conditions will be discussed in up-coming sections.

1.2 Background

Kinetic energy missile systems have been considered by the U.S. Army for use in heavy anti-armor threats since the 1980s. There are several potential advantages of a kinetic energy missile (KEM) over one dependent on chemical explosions to destroy the target. A KEM system is simple. It has no warhead, fuse or onboard sensor to risk malfunction. With less complicated components

the system has the potential of a reduced cost per expended round. The missile is required to travel at hypervelocity speed to impart the necessary kinetic energy to the target. The requirement for this velocity makes for a reduced travel time to target reducing the target's capabilities of intercepting the missile or maneuvering and returning fire. Since 1997 Lockheed Martin has developed two types of kinetic energy missiles, the Line-of-Sight Anti-Tank Weapon (LOSAT) and the Compact Kinetic Energy Missile (CKEM). Neither of the two systems that were developed moved to production, but they are important demonstrators of the capabilities of kinetic energy warheads [5].

1.2.1 LOSAT

The LOSAT warhead is characterized as a "High-density rod armor penetrator." The missile is 112 inches long with a diameter of 6.4 inches. It has a weight of 177 lb. It uses a solid rocket motor developed by Alliant Techsystems (ATK) to propel it to a velocity of 5,000 feet per second and a range of over 4 kilometers. This hypervelocity allows it to reach its maximum range in less than five seconds. Tests of the system proved that it has the capability to accomplish the design goals. During testing it destroyed an M-60 tank moving at 22 mph at 2,400 meters, an incoming tank at 2,400 meters, a moving target in night-time conditions at 4,300 meters, a moving tank at relatively short range, and a

reinforced urban structure. An example of a LOSAT being launched from a modified Humvee is given in Figure 1 [5].

Figure 1: LOSAT Launch [5]

1.2.2 CKEM

The CKEM was a spiral project from the LOSAT. It was designed to be much smaller with an extended range while still delivering devastating effects to the threat. The CKEM is 60 inches long and weighs less than 100 pounds. At a velocity of Mach 6.5+ it has demonstrated extreme lethality and a high probability of first-round kill against all advanced threat armor and hardened bunkers, fortifications, and urban structures. It has an extended range beyond that which tank main guns are capable (5+ kilometers) which gives it a range overmatch [6].

1.3 Previous Work

During the last 5 decades there has been extensive research and work done in developing and refining the finite element method [8]. Due to the abundance of information on the subject much of the past work done in the field will not be covered, only a brief introduction to some of the major breakthroughs in the areas that are relevant to the topic at hand.

1.3.1 Johnson-Cook Constitutive Model

Johnson and Cook recognized that the capabilities of computer codes were becoming limited by not having a simple, accurate model to define the material characteristics for both strength and fracture. They developed their material model to be used in situations of high strains, high strain rates, and high temperatures. The intent was to have a constitutive model that would require only a minimal amount of material constants that can be determined by few experiments. The material constants were determined by purely empirical means. They conducted torsion tests over a wide range of strain rates, static tensile tests, dynamic Hopkinson bar tensile tests, and Hopkinson bar tests at elevated temperatures to gather the data required to determine the appropriate material constants for their constitutive model. The constitutive constants for the tested materials during the model development are given in Table 1.

Table 1: Constitutive Constants for Various Materials [9]

MATERIAL	DESCRIPTION				CONSTITUTIVE CONSTANTS FOR $\sigma = [A + B\epsilon^n][1 + C\ln\dot{\epsilon}^*][1 - T^{*m}]$				
	HARDNESS (ROCKWELL)	DENSITY (kg/m^3)	SPECIFIC HEAT (J/kgK)	MELTING TEMPERATURE (K)	A (MPa)	B (MPa)	n	C	m
OFHC COPPER	F-30	8960	383	1356	90	292	.31	.025	1.09
CARTRIDGE BRASS	F-67	8520	385	1189	112	505	.42	.009	1.68
NICKEL 200	F-79	8900	446	1726	163	648	.33	.006	1.44
ARMCO IRON	F-72	7890	452	1811	175	380	.32	.060	0.55
CARPENTER ELECTRICAL IRON	F-83	7890	452	1811	290	339	.40	.055	0.55
1006 STEEL	F-94	7890	452	1811	350	275	.36	.022	1.00
2024-T351 ALUMINUM	B-75	2770	875	775	265	426	.34	.015	1.00
7039 ALUMINUM	B-76	2770	875	877	337	343	.41	.010	1.00
4340 STEEL	C-30	7830	477	1793	792	510	.26	.014	1.03
S-7 TOOL STEEL	C-50	7750	477	1763	1539	477	.18	.012	1.00
TUNGSTEN ALLOY(.07Ni, .03Fe)	C-47	17000	134	1723	1506	177	.12	.016	1.00
DU-.75Ti	C-45	18600	117	1473	1079	1120	.25	.007	1.00

After completing the model development they evaluated the model and data by comparing their results with data from cylinder impact tests. The evaluation tests conducted provided strains exceeding 2.0 and strain rates exceeding 10^5 sec^{-1}. The results from the cylinder impact tests are given in Figure 2 below [9, 10].

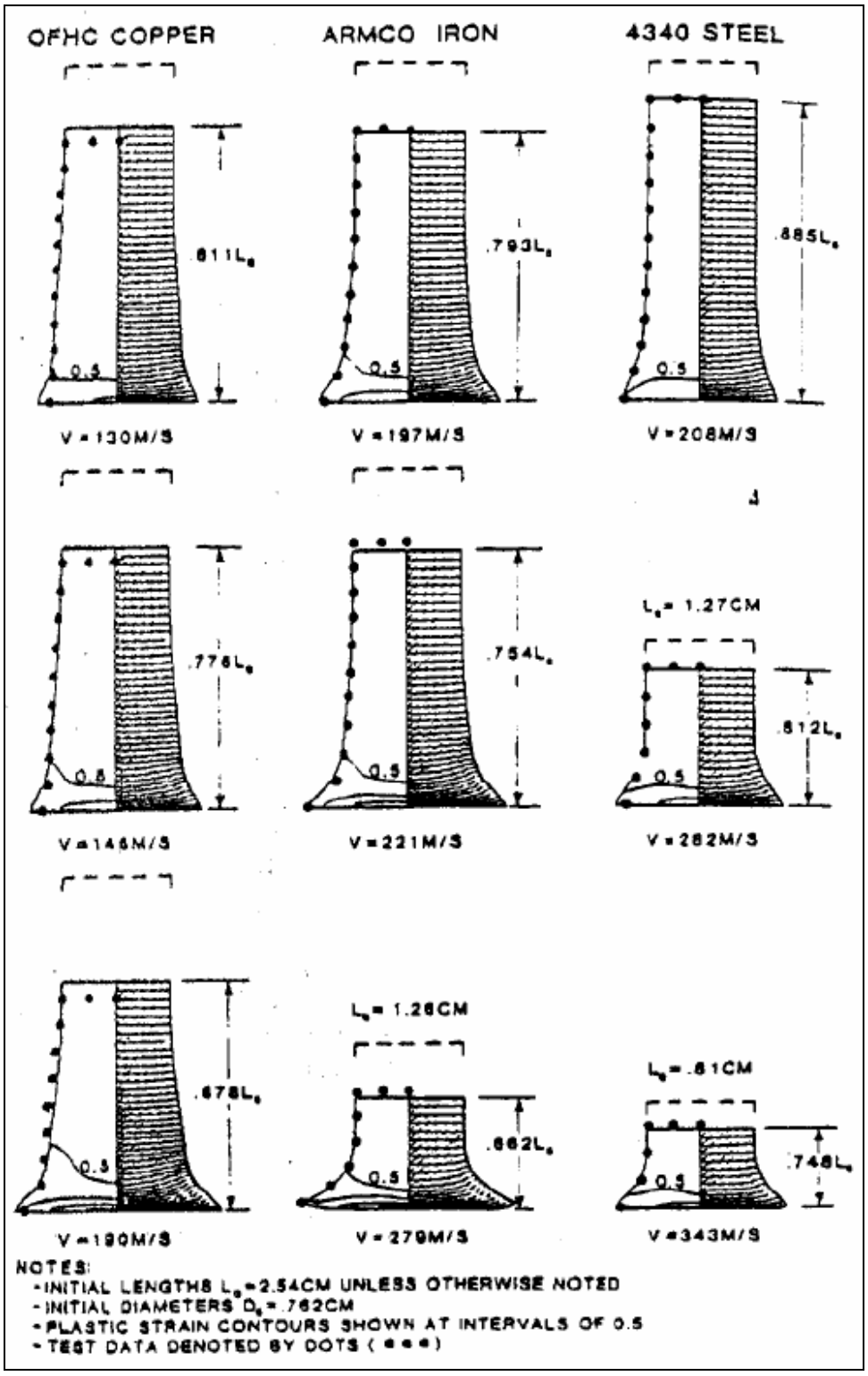

Figure 2: Comparison of Computed Shapes and Test Results for Cylinder Impact Tests at Various Velocities [9]

1.3.2 Failure Modes

Different loading conditions can lead to varied failure mechanisms. Typically one failure mechanism will dominate, though several may contribute to the overall failure of the material. The failure mechanisms or modes that will be discussed are plugging, petaling, and spalling. Examples of these failure modes and others are given in Figure 3 below [11].

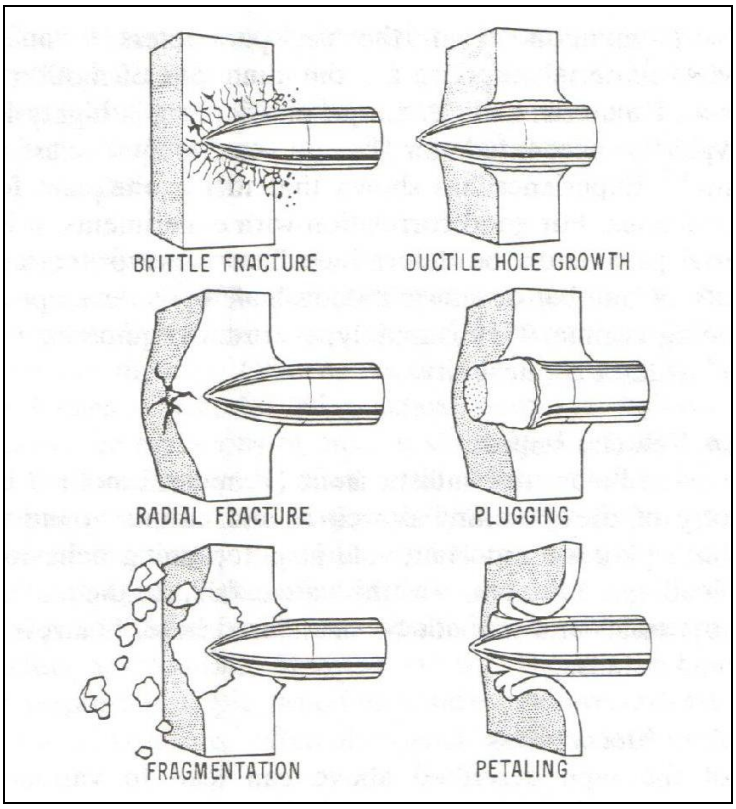

Figure 3: Failure Modes in Impacted Plates [11]

Spalling is defined as a tensile failure that is a result of the interaction of one or more rarefaction waves near any surface except the one the loading is applied. Spallation is a common failure mechanism in hypervelocity impacts, especially when the material is stronger in compression than in tension [11, 12].

Plugging is common when the penetrator has a blunt or hemispherical-nose shape and impacts the target at a velocity close to its ballistic limit. The ballistic limit is the minimum velocity required for penetration. This set of parameters can lead to the formation of a nearly cylindrical slug with a similar diameter to the penetrator being pushed through and ejecting from the target. If the impact velocity exceeds the ballistic limit by more than 5 – 10%, multiple fragments instead of an intact plug will result [11].

Petaling is most common in thin targets being impacted near the ballistic limit. It is caused by high radial and circumferential tensile stresses after the first stress wave passes. Petaling is characterized by star shape cracks that develop around the penetrator nose. The sections separated by the cracks are then pushed back by the penetrator as it passes through the target. The result is a petal shape to the fractured surface [11].

1.3.3 Shock Wave Propagation

A uniaxial stress-strain curve that will be used to describe the motion and development of shock waves in a solid is given in Figure 4.

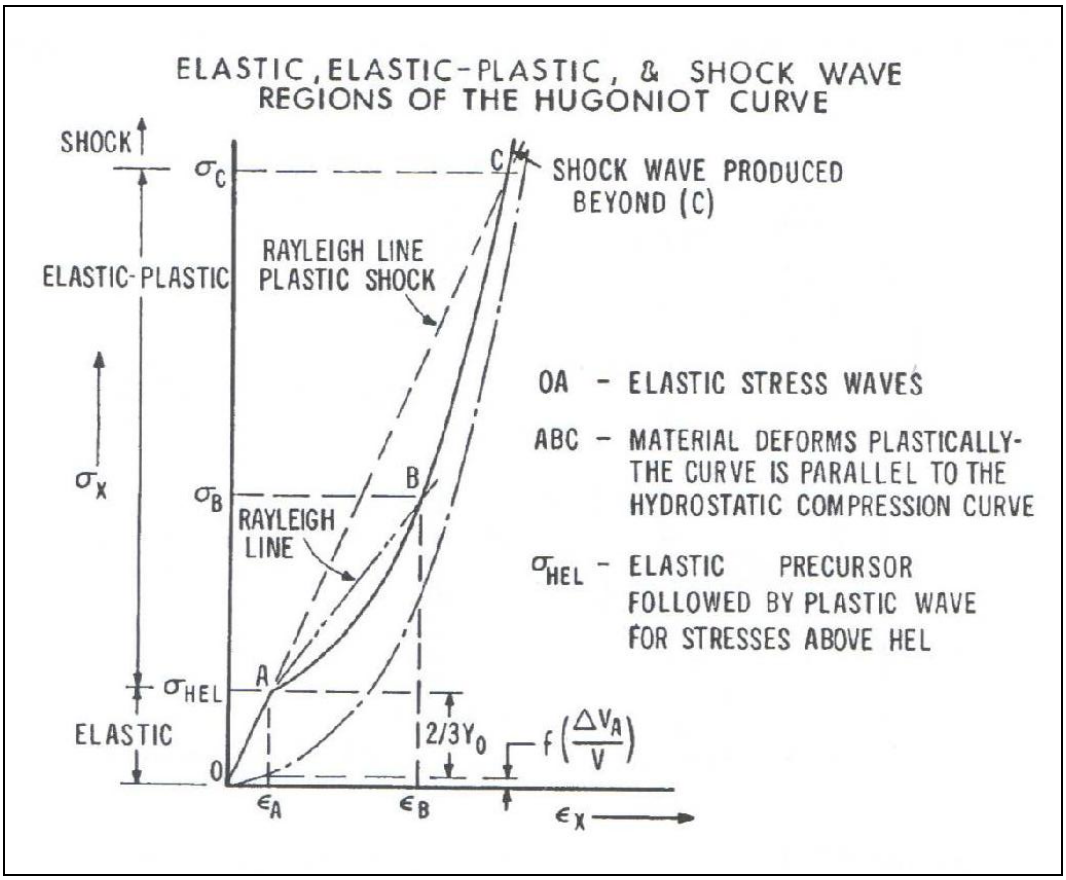

Figure 4: Regions of Elastic, Elasto-Plastic, and Shock Wave Propagation [12]

Uniaxial strain can be described as deformation that is restricted to one dimension. The importance of the uniaxial stress-strain curve given is that it indicates the stress at which multiple stress waves exist in the material. This stress is referred to as the Hugoniot elastic limit which is defined as the maximum stress for 1D elastic wave propagation in plate geometries and is written as σ_{HEL}. Above σ_{HEL} the elastic wave will move with a speed

$$C_E^2 = \frac{E(1-v)}{\rho_0(1-2v)(1-v)} \tag{8}$$

Following the elastic wave will be one or more plastic waves each with a velocity

$$C_p = \sqrt{\frac{1}{\rho_0}\frac{d\sigma}{d\varepsilon}} \tag{9}$$

Above σ_c strong shock waves can occur. In this region materials display characteristics similar to fluids [12].

The high-pressure wave builds up to a shock wave due to the differences of the pressure-density relationships in different regions. The pressure and density are linearly related in the elastic region. Above the elastic region they are not linearly proportional and the wave velocity increases with pressure or density. Figure 5 is an illustration of a propagating high-pressure wave. At point A in this illustration, the pressure is low and the wave velocity is low. At point B the velocity is higher because above the elastic limit the wave velocity increases with increasing pressure. At point C the wave velocity is even higher than at point B.

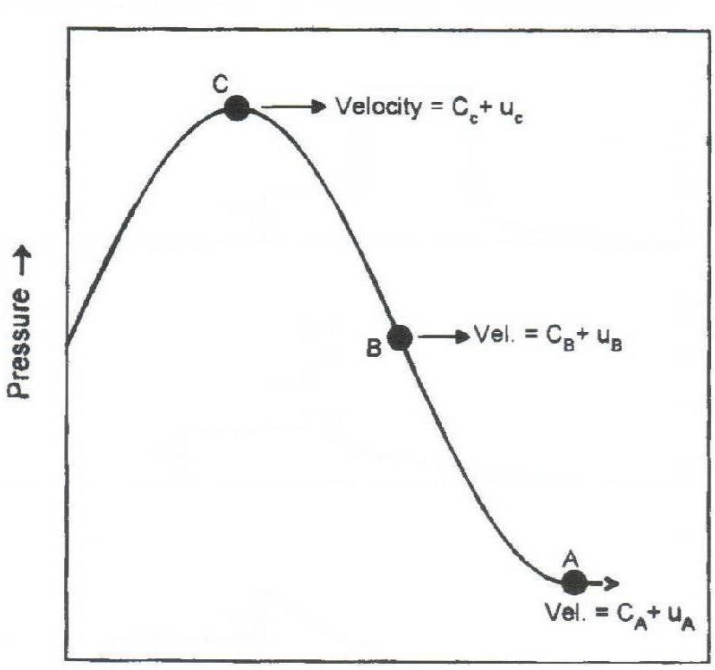

Figure 5: Propagating High-Pressure Wave [12]

Figure 6 shows the wave continuing to steepen until it eventually reaches a vertical orientation. When the wave becomes a vertical front it is considered a shock wave. Instead of the once present smooth transition of matter in front of the wave to matter past the wave, now there is a discontinuity between the shocked and un-shocked material [12].

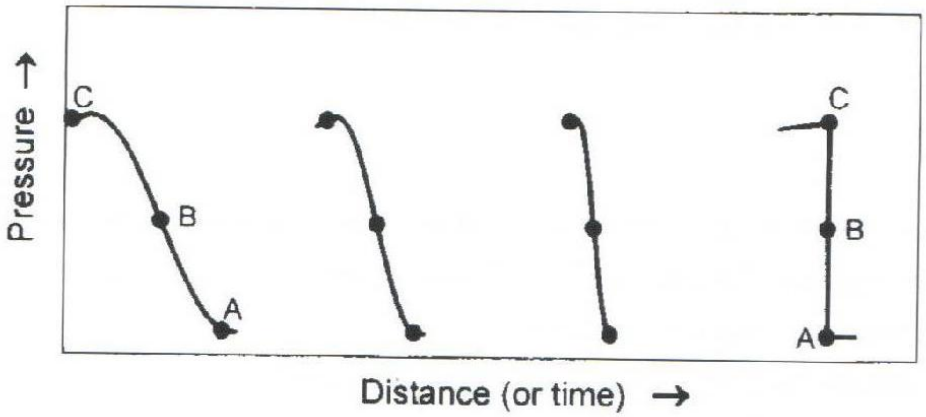

Figure 6: Buildup of a Pressure Wave to a Shock Wave [12]

Chapter 2: Model Theory and Setup

2.1 Explicit Non-Linear Solver

MSC-Dytran was the explicit non-linear finite element analysis solver used in the current simulations. An explicit solver has an advantage over the more commonly used implicit solver in simulations when a very small time step is required. A small time step may be required for one of the following reasons: material nonlinearity, large geometric nonlinearity, when it is necessary to recover stress wave effects, and when the body undergoes large displacements. Explicit solutions are better suited than implicit solutions for analysis requiring small time steps as well as large problems because matrix decompositions or matrix equation solutions are not necessary. The flow diagram as seen on Figure 7 illustrates the loop that is carried out for each explicit time step [13].

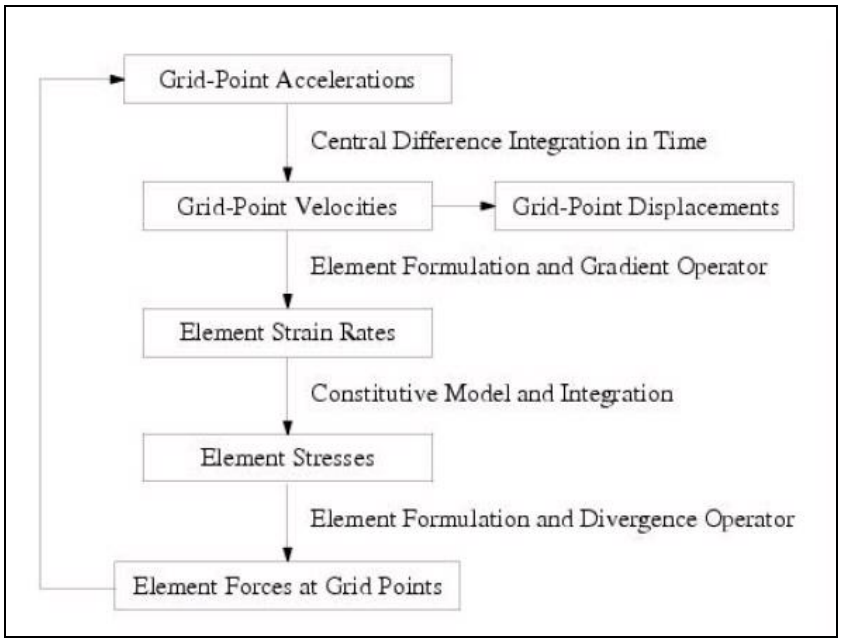

Figure 7: Explicit Time Step Loop [13]

Figure 8 gives an indication of the differences in efficiency and costs between an implicit and explicit solution due to nonlinearities and problem size [14].

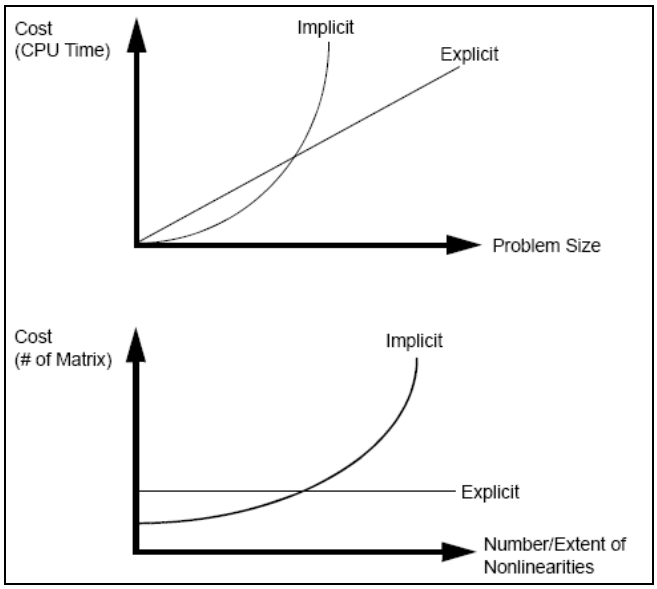

Figure 8: Explicit vs. Implicit Efficiency and Cost Comparison [14]

2.2 Lagrangian Solver

The Lagrangian solver calculates the motion of elements which have constant mass. This is accomplished by fixing grid points, also referred to as nodes, to locations on the geometric body that is to be analyzed. By connecting the nodes together, elements are created. A collection of elements is a mesh. The nodes move and the elements distort as the body deforms. The Lagrangian solver is used to model the solid materials required for the simulations being investigated. An example of a Lagrangian mesh undergoing distortion is given in Figure 9 [13].

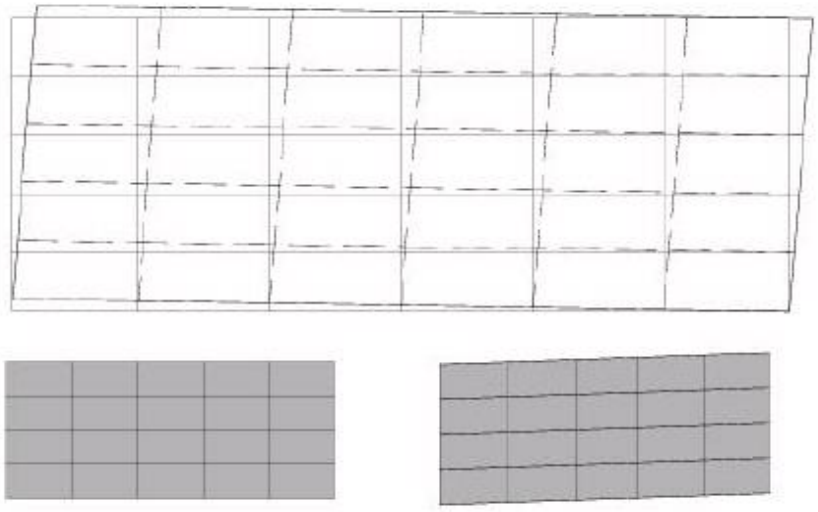

Figure 9: Lagrangian Mesh [13]

2.3 Eulerian Solver

The Eulerian solver calculates the motion of material through elements of constant volume. Instead of the nodes moving with the body they are fixed in space. The mesh then becomes a "fixed frame of reference" that the mass, momentum, and energy of the material of the body being analyzed moves through. The Eulerian solver is used to model the fluid materials for the simulations being investigated. An example of the transportation of material through an Eulerian mesh is given in Figure 10 [13].

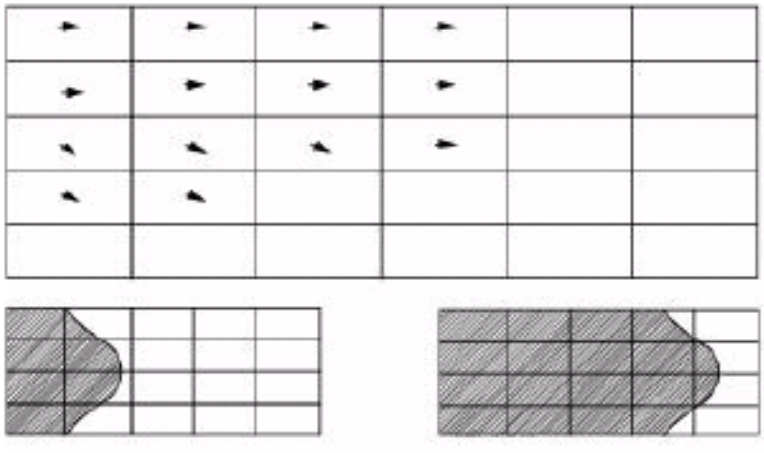

Figure 10: Eulerian Mesh [13]

2.4 Geometry

The geometry for the finite element analysis was created with MSC.Patran which is the Pre- and Post-Processor used. The target and penetrator were modeled as closely to the experimental specifications as possible. Drawings of the penetrator and target can be seen in Figure 11 and Figure 12 respectively [15].

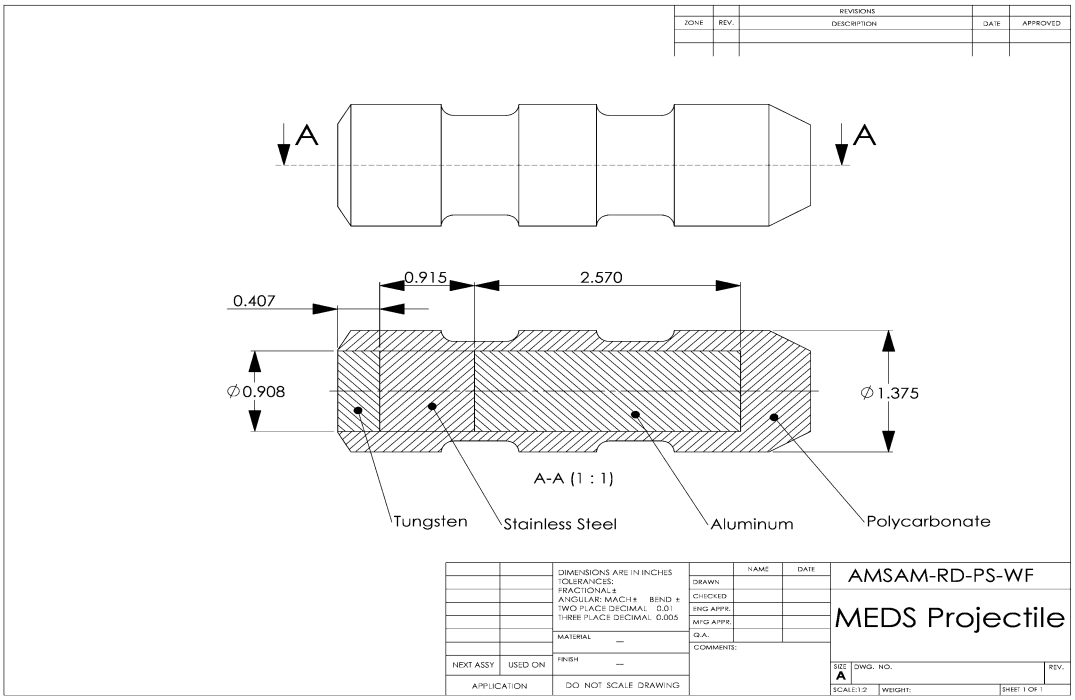

Figure 11: Penetrator Drawing [15]

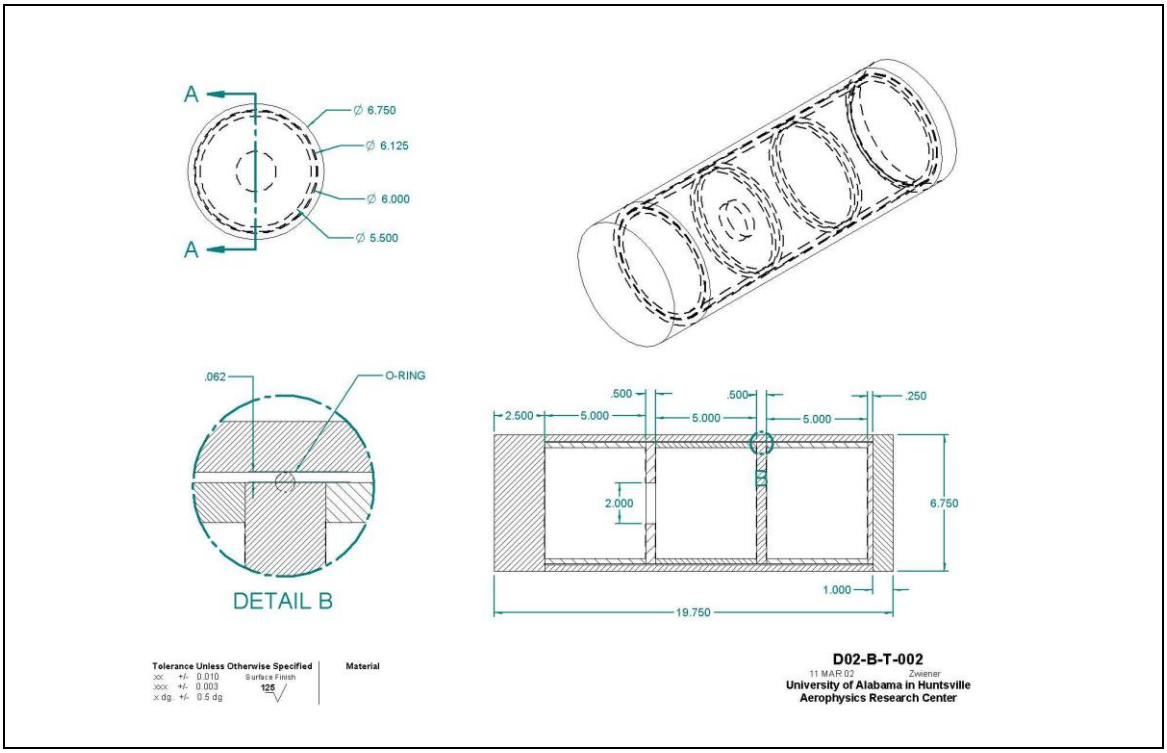

Figure 12: Target Drawing [15]

2.4.1 Penetrator

The cylindrical penetrator was made of three different metallic sections of equal mass encased in a polycarbonate shell. The penetrator is given in Figure 13 below.

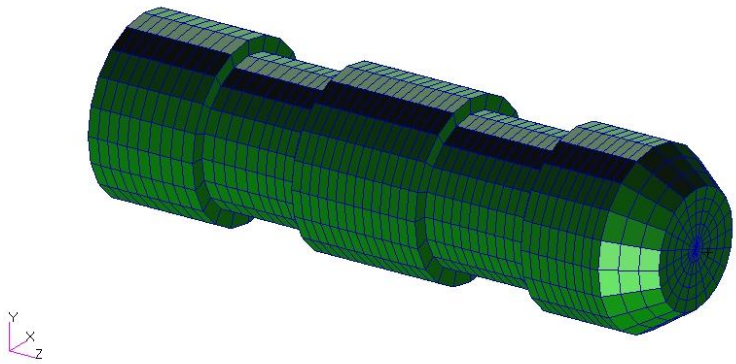

Figure 13: Complete Penetrator

The diameter of each section is 0.908 inch. The metallic sections are tungsten, steel, and aluminum. The tungsten section has a length of 0.407 inch. The steel section has a length of 0.915 inch. The aluminum section has a length of 2.57 inches. The polycarbonate shell was made of Zytel. The zytel case has maximum outside diameter of 1.375 inches and a length of approximately 4.563 inches. The order of the metallic sections was varied to identify the configuration that distributes the most energy to the target. Two configurations will be discussed in this work. These are referred to as Aluminum-Steel-Tungsten (AST), where the aluminum section impacts first followed by the steel

then the tungsten, and Tungsten-Steel-Aluminum (TSA), where the tungsten section impacts first followed by the steel then the aluminum [15].

2.4.2 Target

The cylindrical target was made of steel and was designed to represent three separate sections which are segmented with a bulkhead with a hole in the center and a solid bulkhead. The target is given in Figure 14 below.

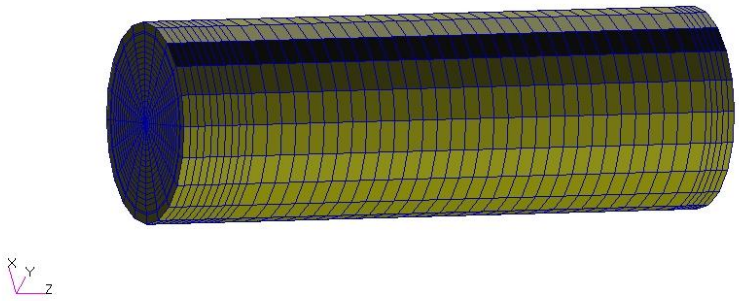

Figure 14: Target

It consists of a front plate which at 2.5 inches thick is five times as thick as the interior bulkheads and two and a half times as thick as the rear plate. This differential in the thicknesses simulates the difference between interior walls and the exterior plating found in many armored vehicles. The plates and bulkheads are bound by two tubes which will be referred to as walls. These two walls are separated by a distance of 0.0625 inch. The inner wall with a thickness of 0.25 inch attaches the bulkheads to the front plate and back plate. The outer wall

with a thickness of 0.3125 inch attaches the front plate to the rear plate. The overall length of the target is 19.75 inches and has a diameter of 6.75 inches [15].

2.5 Elements

CHEXA elements are used throughout the model to construct the solid Lagrangian and Eulerian elements whenever possible. CPENTA elements are used as necessary to fill in the gaps left by the CHEXA elements. CHEXA is a six-sided solid element with eight grid points. CPENTA is a five-sided solid element with six grid points. The coupling surfaces require the use of shell elements. For these, CQUAD4 elements were used whenever possible and CTRIA3 were used when necessary to fill the gaps left by the CQUAD4 elements. CQUAD4 is a quadrilateral shell element with four grid points. CTRIA3 is a triangular shell element with three grid points. The next sections will highlight the steps taken to mesh each part of the model.

2.5.1 Penetrator

The metallic sections of the penetrator are all meshed with 20 elements on the circumference and 5 elements in the radial direction. The tungsten section which was meshed with 5 elements along the length of the rod and contains 500 elements and 606 nodes is given in Figure 15.

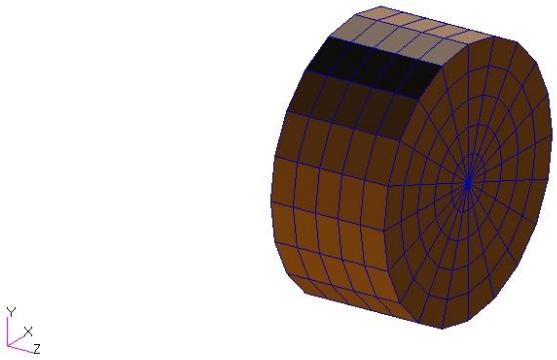

Figure 15: Tungsten Section of the Penetrator

The steel section which has 10 elements along the length of the rod and contains 1000 elements and 1111 nodes is given as Figure 16.

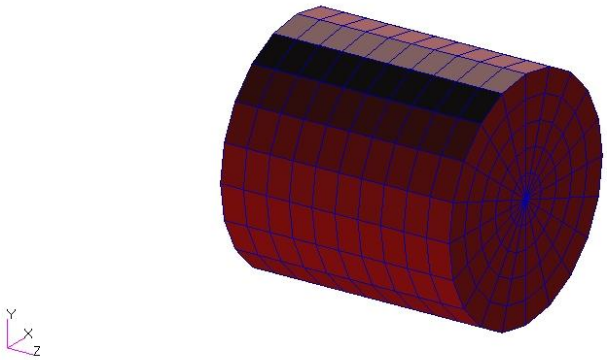

Figure 16: Steel Section of the Penetrator

The aluminum section which has 35 elements along the length of the rod and contains 3500 elements and 3636 nodes is given in Figure 17.

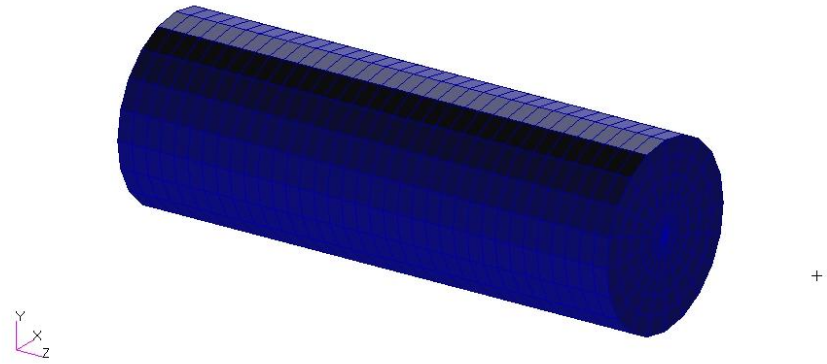

Figure 17: Aluminum Section of the Penetrator

The zytel was meshed to match the corresponding metallic section encased and consists of 2560 elements and 3809 nodes. A rear view of the zytel section is given below as Figure 18.

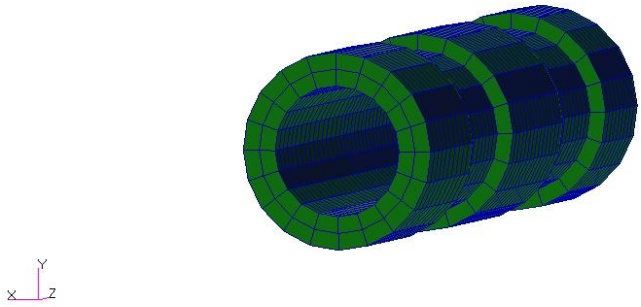

Figure 18: Rear View of Zytel Penetrator Shell

Figure 19 and Figure 20 given below shows the AST and TSA penetrator configurations. It is important to note that the direction of travel is along the positive Z axis.

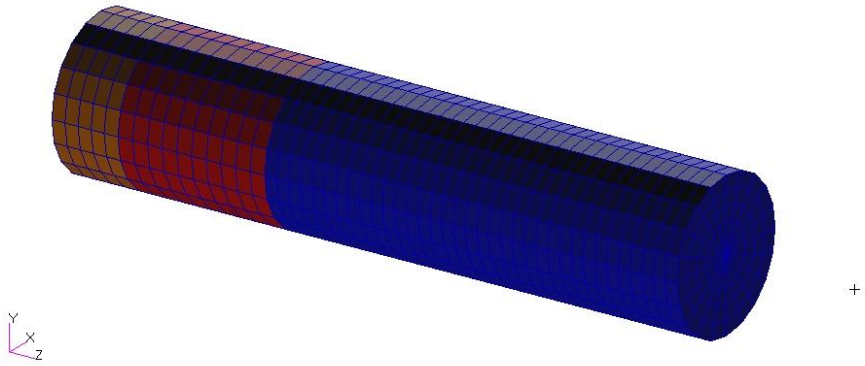

Figure 19: AST Penetrator Configuration Excluding Zytel Shell

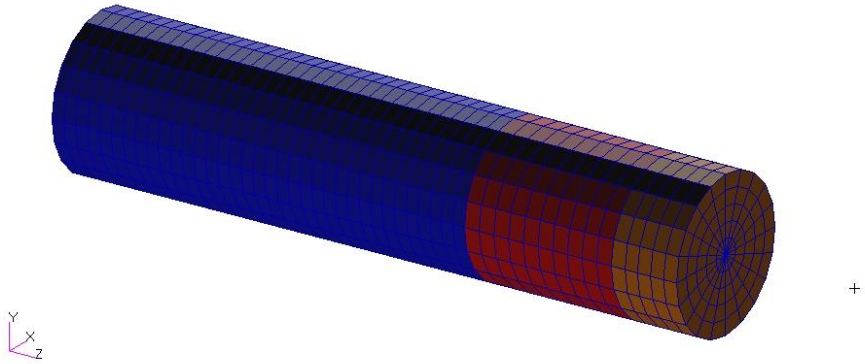

Figure 20: TSA Penetrator Configuration Excluding Zytel Shell

2.5.2 Target

The front and rear plates were created using four different solids and then meshed separately. This was to ensure the appropriate walls mated correctly and the distance between the walls is properly accounted for. Each piece of the target was meshed with 20 elements along the circumference. The center section of the front plate, rear plate, and solid bulkheads are meshed with 15 elements in the radial direction. The bulkhead with the hole in the center was meshed with

10 elements in the radial direction. All of the outer rings of the target pieces are meshed with 1 element in the radial direction. The front plate which was meshed with 10 elements along its length or thickness and consists of 3600 elements and 3971 nodes is given in Figure 21.

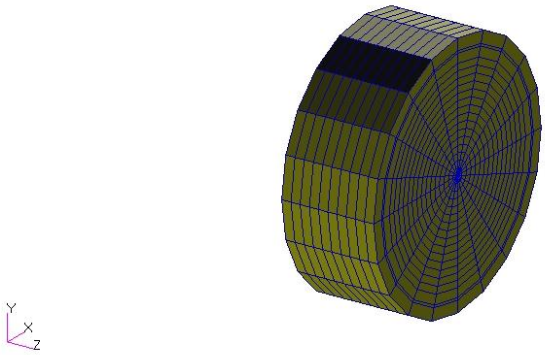

Figure 21: Front Plate

The rear plate which was meshed with 5 elements along its length or thickness and consists of 1800 elements and 2166 nodes is given in Figure 22.

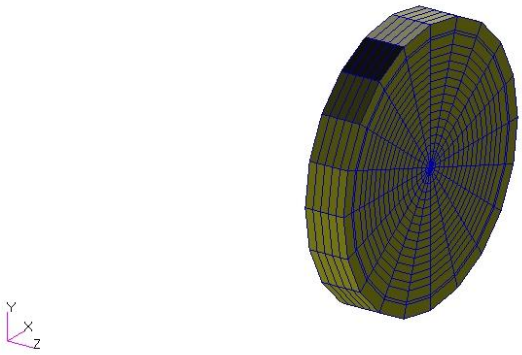

Figure 22: Rear Plate

The bulkheads which were each meshed with one element along their length or thickness and consist of a total of 860 elements and 1764 nodes are given in Figure 23.

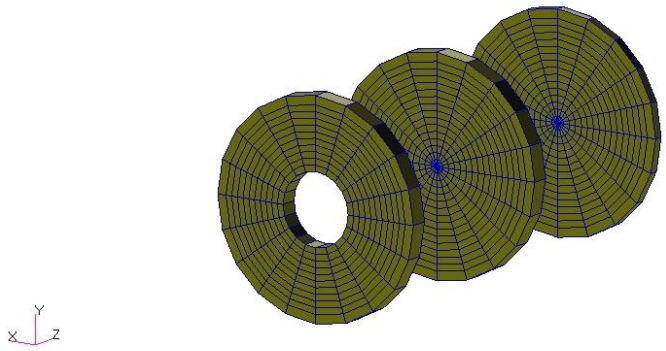

Figure 23: Bulkheads

The inside and outside walls were meshed with one element in the radial direction and twenty elements along the circumference. The inside wall was made of three separate sections, each meshed with 10 elements along their length. This results in a total of 600 elements and 1320 nodes for these sections. The inside walls are given in Figure 24.

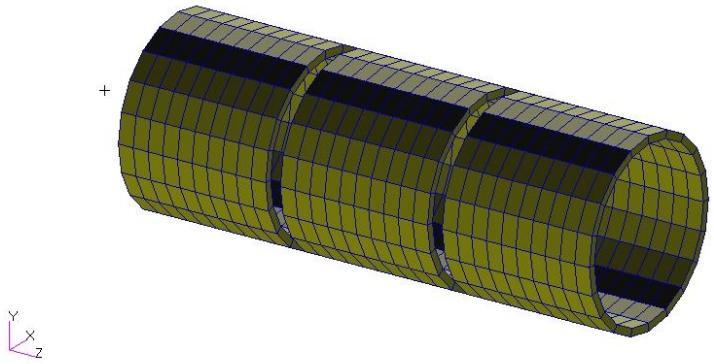

Figure 24: Inside Walls

The outside wall is one solid piece and was meshed with 32 elements along its length giving it a total of 640 elements and 1320 nodes. It is given below in Figure 25.

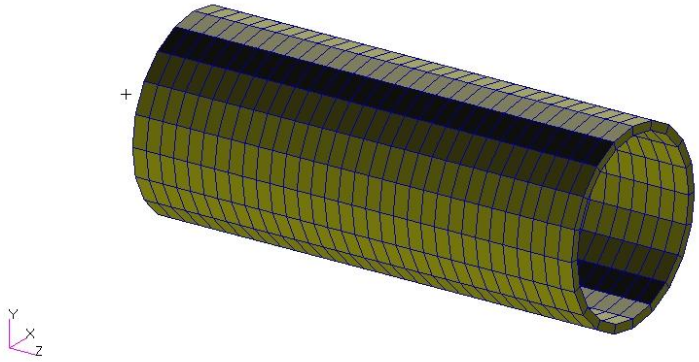

Figure 25: Outside Wall

To give a perspective on the section sizes relative to the complete model, the target pieces assembled are shown in Figure 26 through Figure 28. Figure 26 shows the front plate, rear plate, and bulkheads. Figure 27 shows the front plate,

rear plate, bulkheads, and inside walls. Figure 28 shows the complete target and penetrator

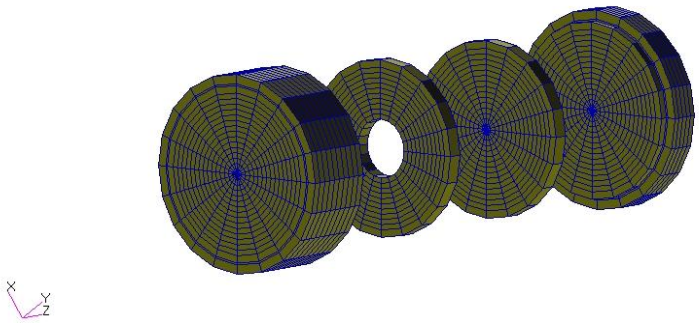

Figure 26: Front Plate, Bulkheads, and Rear Plate

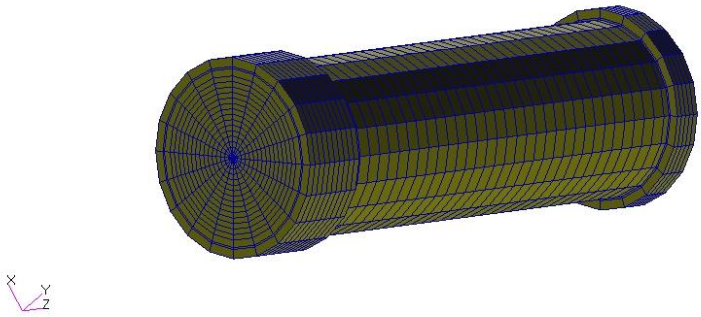

Figure 27: Plates, Bulkheads, and Inside Walls

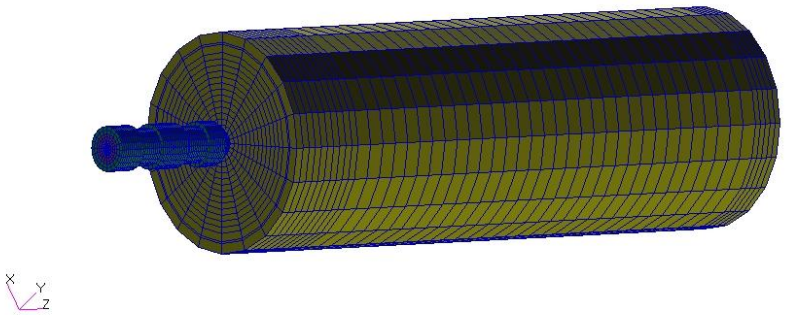

Figure 28: Penetrator and Target

2.5.3 Coupling Surfaces

To couple the Euler elements to the Lagrangian elements, "dummy" surfaces were used. Coupling surfaces have no properties or thickness assigned to them. This is a feature of the solver to allow surfaces to be defined for the transfer of the energy, mass, and momentum from one element type to the other. The coupling surfaces were grouped into 2 separate sections to correspond to the 2 interior Euler regions. The first section coupled the two target compartments connected by the bulkhead with a hole in the center to their corresponding Euler region. The first section was also used to couple the interior Euler regions to the exterior Euler region. The second section coupled the target compartment separated by the solid bulkhead and rear plate to its corresponding Euler region. Each section was meshed to match the Lagrangian solid it coupled. There were a total of 2240 elements and 2264 nodes that made up the coupling surfaces. A

further discussion of the Euler regions will be given in the coming sections. Two views of the coupling surfaces are given in Figure 29 and Figure 30.

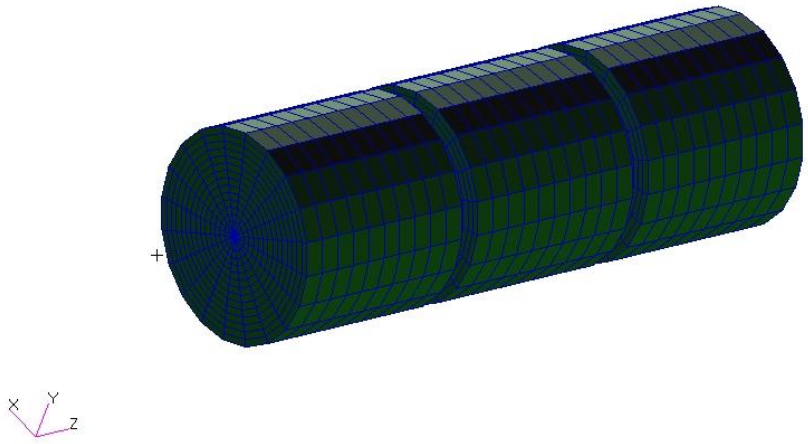

Figure 29: Coupling Surfaces, View 1

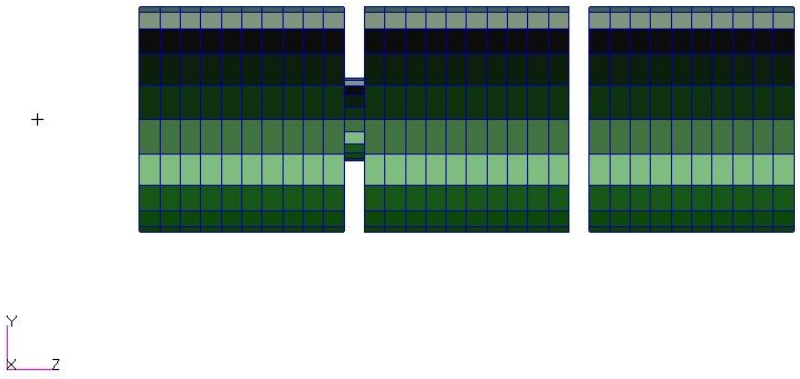

Figure 30: Coupling Surfaces, View 2

2.5.4 Fluid

The Euler regions were constructed using the mesh box feature of the solver. This control allows the user to construct the Euler region by specifying the

origin, length of the region in each coordinate direction, and the number of elements in each coordinate direction. The first interior Euler region began at 0.1 inch before the target front plate ends and extends to 0.1 inch after the solid bulkhead begins. The second interior Euler region began at 0.1 inch before the solid bulkhead ends and extends to 0.1 inch after the rear plate began. The exterior Euler region began at 27.4 inches before the front plate began and extends to 0.1 inch after the front plate ends. The first interior Euler region was meshed with a total of 16,800 elements and 18,963 nodes. The second interior Euler region was meshed with 8,000 elements and 9,261 nodes. The exterior Euler region is meshed with 32,000 elements and 35,301 nodes. The interior Euler regions covering their corresponding coupling surfaces are given in Figure 31. The exterior and interior Euler regions together are given in Figure 32.

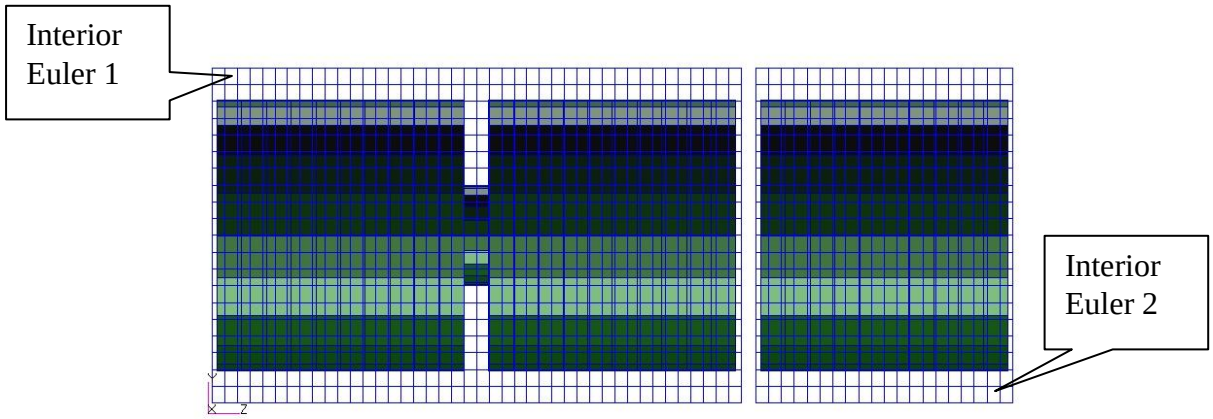

Figure 31: Interior Euler Regions and Coupling Surfaces

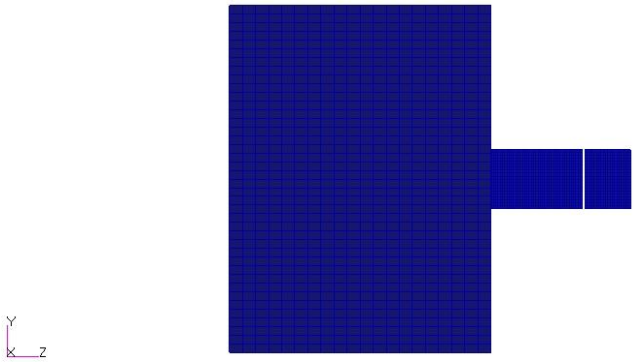

Figure 32: Euler Regions

2.6 Solid Material Models and Properties

Four different materials were used to model the penetrator and target. 4340 steel was used for the steel sections of the penetrator and for the entire target. The other metallic sections of the penetrator consist of tungsten (0.07 Ni, 0.03 Fe) and 6061-T6 aluminum. The polycarbonate shell that holds the penetrator together is constructed from zytel, a material manufactured by Dupont. All material values which will be discussed in more detail in the following paragraphs were given by Foster [15].

The material properties were input into the solver via a constitutive model. A complete constitutive model consists of a combination of an equation of state, a shear model, a yield model, a failure model, and a spallation model [4]. The equation of state, shear model, yield model, failure model, and spallation model used will be discussed in more detail in the coming sections.

The polynomial equation of state was used for all solid materials to define the hydrodynamic volume limit. This was necessary due to the hydrodynamic volume failure being used. More details concerning the hydrodynamic volume failure will be discussed in the failure model section.

The elastic shear model, SHREL, which was used for each material has a constant shear modulus. The shear modulus used in this analysis is the slope of the linear relationship between the shear stress and strain.

The von Mises yield model was used for the zytel. This model when used with solids is considered an elastic perfectly plastic yield model, no strain hardening present, therefore only the yield stress is required. The Zytel yield stress, shear modulus, and other material properties are given in Table 2.

Table 2: Misc. Material Properties

Material	G (psi)	σ_{yield} (psi)	K (psi)	MPS (in/in)	PMIN (psi)	ρ (lb_sec^4/in^4)
Aluminum (6061-T6)	4.0000E+06	N/A	N/A	1.00	-1.74E+05	2.530E-04
Steel (4340)	1.1618E+07	N/A	N/A	1.25	-4.64E+05	7.320E-04
Tungsten (0.07 Ni, 0.03 Fe)	2.3206E+07	N/A	N/A	0.75	-1.31E+05	1.589E-03
Zytel	1.1100E+05	6.9E+03	2.4E+05	0.33	N/A	1.002E-04

The Johnson-Cook yield model was used for every material with the exception of the zytel. This yield model is denoted in the solver by the YLDJC entry. The yield stress is calculated as a function of the plastic strain, strain rate, and temperature. The Johnson-Cook yield stress equation and variable

definitions are given below in Figure 33 [13]. The Johnson-Cook constants and other material properties used for each material are given in Table 3.

$$\sigma_y = (A + B\varepsilon_p^n)(1 + C\ln(\dot{\varepsilon}/\dot{\varepsilon}_0))(1 - T^{*m})$$

T^*	=	$\frac{(T - T_r)}{(T_m - T_r)}$
ε_p	=	effective plastic strain
$\dot{\varepsilon}$	=	effective strain rate
$\dot{\varepsilon}_0$	=	reference strain rate
T	=	temperature
T_r	=	room temperature
T_m	=	melt temperature

A, B, n, C, and m are constants.

Figure 33: Johnson-Cook Yield Model [13]

Table 3: Material Properties and Constants for Johnson-Cook Yield Model

Material	A (psi)	B (psi)	n	C	m	EPS0 (in/in/sec)	CP (in²/sec²-°R)	TMELT (°R)	TROOM (°R)
Aluminum (6061-T6)	4.700E+04	1.650E+04	0.42	2.0E-03	1.34	1.0	7.1717E+04	1666	530
Steel (4340)	1.149E+05	7.390E+04	0.26	1.4E-02	1.03	1.0	4.1140E+05	3228	530
Tungsten (0.07 Ni, 0.03 Fe)	2.184E+05	2.560E+04	0.12	1.6E-02	1.00	1.0	1.1580E+05	3102	530

2.7 Fluid Material Models, Properties, and Initial Conditions

Air is the material used in the fluid sections. A single material, HYDRO constitutive model was utilized. This material model uses the gamma law equation of state to calculate the pressure. The material is defined by the specific internal energy and density. From these two values and the ratio of specific heats, pressure can be calculated using the following formula:

$$P = (\gamma-1)\varrho e \quad (10)$$

where e is the specific internal energy per unit mass, ϱ is the overall material density, γ is the ratio of specific heats [13]. The property values used as well as the initial conditions for the air that were used can be found in Table 4.

Table 4: Air Properties

γ	CV (in^2/s^2/R)	e (in^2/sec^2)	ϱ (lbf_s^2/in^4)
1.4	6.12901E+05	3.30208386192E+08	1.12297E-07

2.8 Boundary Conditions and Initial Velocity

The target is constrained at a point on the outer radius, centered between the two edges of the front plate and at a point on the outer radius, centered between the two edges of the rear plate. These constraints restrict translation in any direction. Figure 34 shows the constraints placed on the front and rear plates. The penetrator was given an initial velocity of 70,866 in/sec in the positive Z coordinate direction [15].

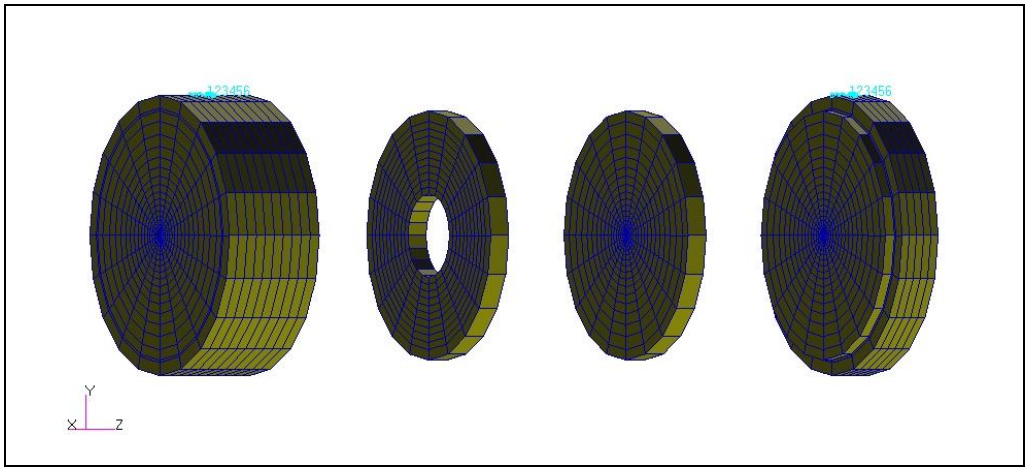

Figure 34: Boundary Conditions on Plates

2.9 Contact

The solver's master-slave contact algorithm was used to define the contact between the penetrator and target. The monitoring side, search algorithm, adaptive setting, initial penetration, and slave node deactivation were all enabled in the contact algorithm.

The monitoring side was set to BOTH. This allows the solver to set the penetration side of the element to the side which the slave node approaches the master face.

The FULL search algorithm was used. This setting results in all the faces of the master surface being considered when the search for the closest master face for a slave node is performed. The slave node's search for the closest master surface is done by a normal projection of the slave node on the faces of the master surface. The FULL option is the most reliable of the available options, but is the most computational expensive, however, the computational expense was not a burden in this simulation.

The adaptive setting was set to YES. In The solver the adaptive setting determines how the master surfaces react to element failure. For Lagrangian solids the free faces are active initially and the internal faces are deactivated. When an element fails, it is possible that some of the internal faces may become free faces. If that is the case the newly defined free faces then become active.

After all the elements connected to a master face have failed, it then is deactivated throughout the rest of the analysis. This logic is ideal for modeling penetration phenomena, and is also referred to as "eroding contact."

The initial penetration allows the slave node to penetrate the master surface up to a set tolerance at the beginning of an analysis. The solver's default of 1.E20 was used as the tolerance for this analysis.

METHOD3A was the slave node deactivation method used in this analysis. This method sets the nodes active as slaves from the beginning of the analysis regardless if they reside on the inside or the outside of the mesh. This also allows for the nodes of the master surface to act as slaves once they reside on the outside of the mesh. After all the connected elements have failed the nodes are deactivated as slaves [16].

2.10 Coupling Algorithm

The solver's general coupling algorithm was used with the addition of the failure definition that allows the Euler regions to interact and transfer material between regions when the coupling surfaces fail. The model was created with all coupling surfaces having a failure definition, but the only one that utilized this function in the simulation was the coupling surface attached to the back of the front plate as this was the only region of failure in the target.

2.11 Failure Models

The maximum plastic strain and hydrodynamic volume limit failure models were used for all materials. The spallation pressure failure model was used for all materials except the zytel.

The maximum plastic strain failure model was defined in the material constitutive model via the FAILMPS entry. When using this model the material fails completely when the plastic strain exceeds the given limit [13]. The assumed maximum plastic strains for aluminum was 1.0, steel was 1.25, tungsten was 0.75, and zytel was 0.33 [15].

The solver's default hydrodynamic volume limit of 1.1 was used for each material. The hydrodynamic volume failure model will cause the elements with a relative volume, defined as the reference density divided by the actual density, greater than the limit to fail completely. Once the element fails the stress state is set to zero [16].

The solver uses a constant minimum pressure method to determine if an element spalls. The solver defines the positive pressures as compression, therefore the minimum spallation pressure must be less than or equal to zero. If the pressure in an element falls below the minimum set limit, the element spalls and the pressure and yield stress are set to zero. At this point the material acts like a fluid. At the point the pressure rises above zero, the material is no longer

in a spalled state. The cycle then can repeat with the pressure decreasing to the specified minimum and spallation occurring again [13].

Chapter 3: Results

Due to the different nature of the fluid that was modeled in the Euler region and the solid materials modeled in the Lagrangian sections these results will be discussed and presented in separate sections.

3.1 Lagrangian Results

There are three different types of results presented for the Lagrangian elements. These consist of time history graphs, energy of distortion contour plots, displacement contour plots and effective stress fringe plots. An explanation of each will be given in the following paragraphs.

The first set of results given is the material time history plots for each penetrator configuration (AST and TSA). These plots show the energy of distortion, kinetic energy, internal energy, and momentum in all three coordinate directions for each material as a function of time. The time history plots given below were compared to Foster's results to gain confidence the Lagrangian sections were properly constructed before the Euler regions and fluid structure coupling were added. It was found through this comparison that the trends were similar. Foster's results are shown in the Appendix.

The energy of distortion for a material is the sum of the distortional energy of all the elements that are in that material. The distortional energy for one element is defined as the sum (in time) of deviatoric stresses (a measure of the shearing

exerted by a state of stress [17]) multiplied by the strain increments multiplied by the change in time [18]. Figure 35 and Figure 36 shows the Energy of Distortion vs. Time plot of each material for both penetrator configurations. The small increase in the target energy of distortion at approximately 0.00025 second was found to be the result of a piece of the aluminum that survived the impact with the front plate striking the solid bulkhead.

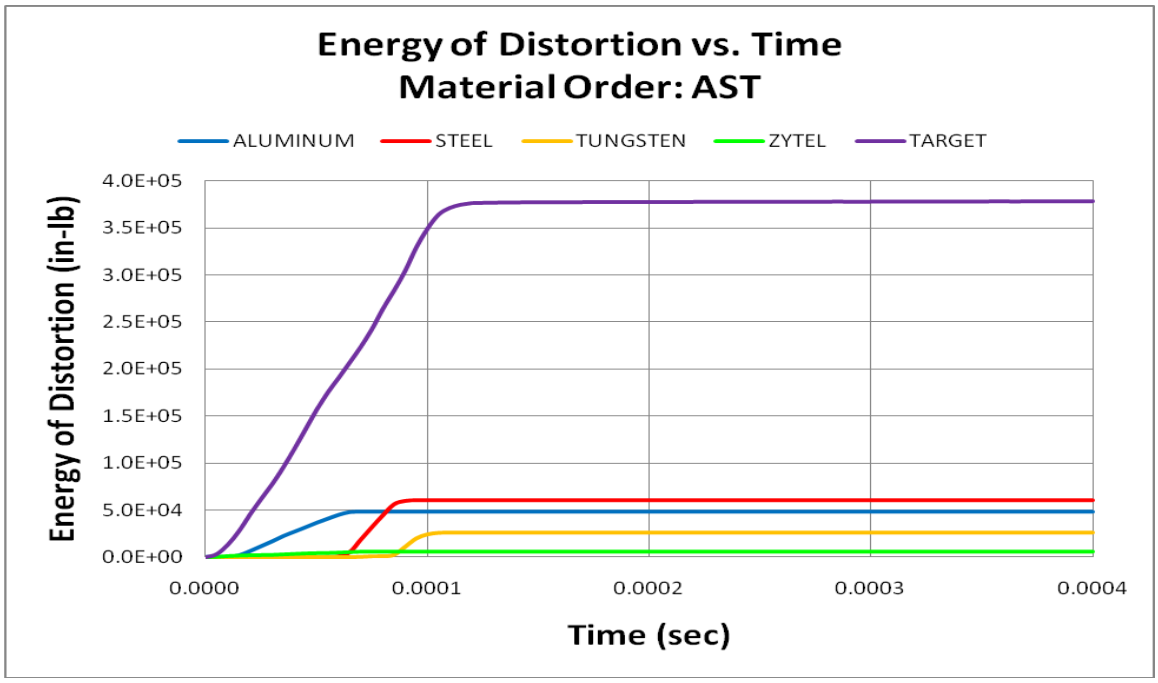

Figure 35: AST Energy of Distortion vs. Time

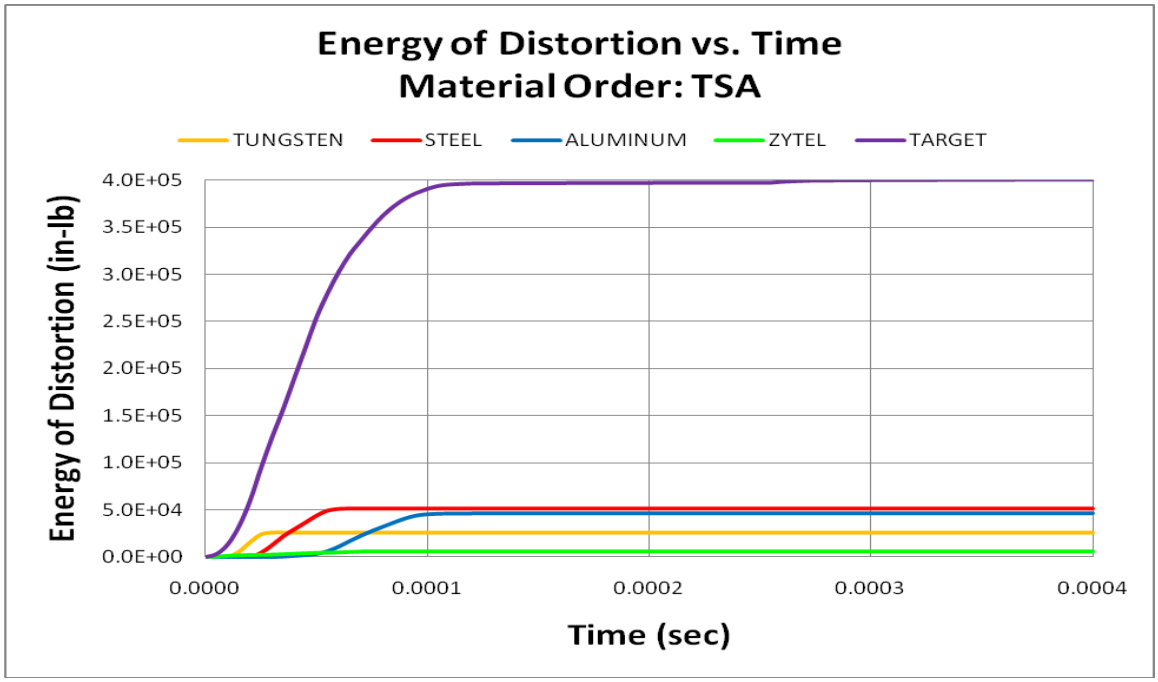

Figure 36: TSA Energy of Distortion vs. Time

For ease of comparison of the penetrator configurations with and without the fluid the distortional energy curves are given in the following plots. Figure 37 shows the distortional energy of the target. Figure 38 shows the distortional energy of the complete penetrator. This is calculated by summing the energy of distortion for the tungsten, steel, aluminum, and zytel sections. It can be seen from these figures that the target incurs a larger distortional energy when the penetrator is in the TSA configuration, but the penetrator incurs a larger distortional energy when it is in the AST configuration. This work also shows that there is minimal difference in the penetrator distortional energy when the fluid is applied to the model.

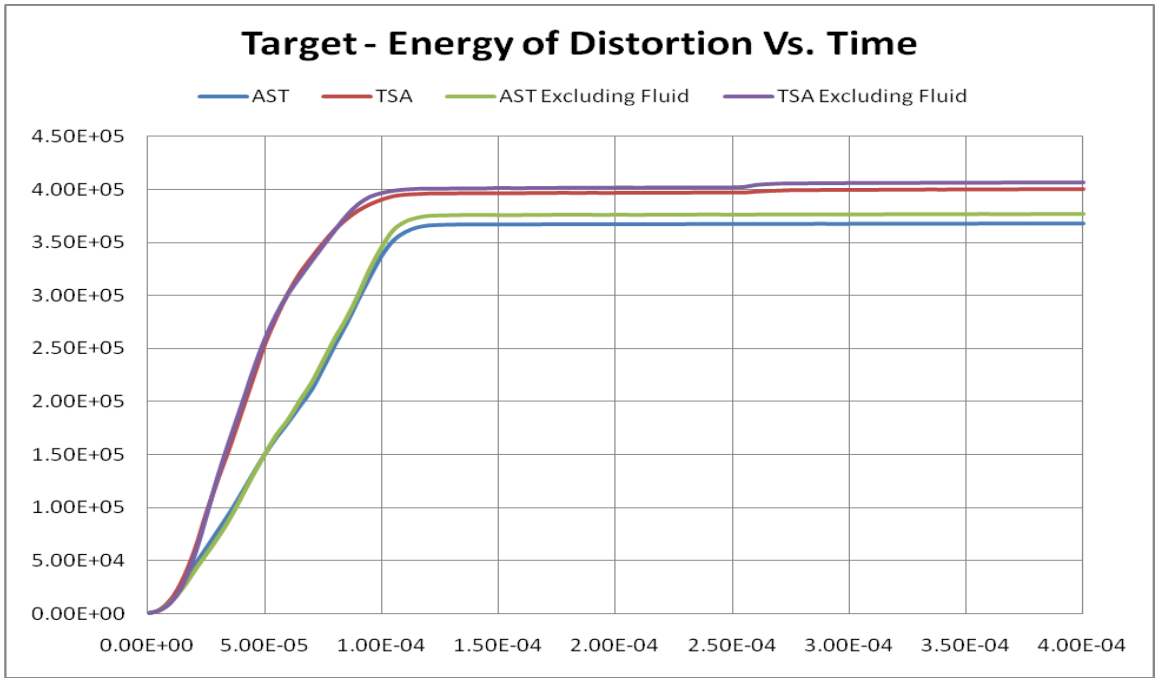

Figure 37: Target Energy of Distortion vs. Time

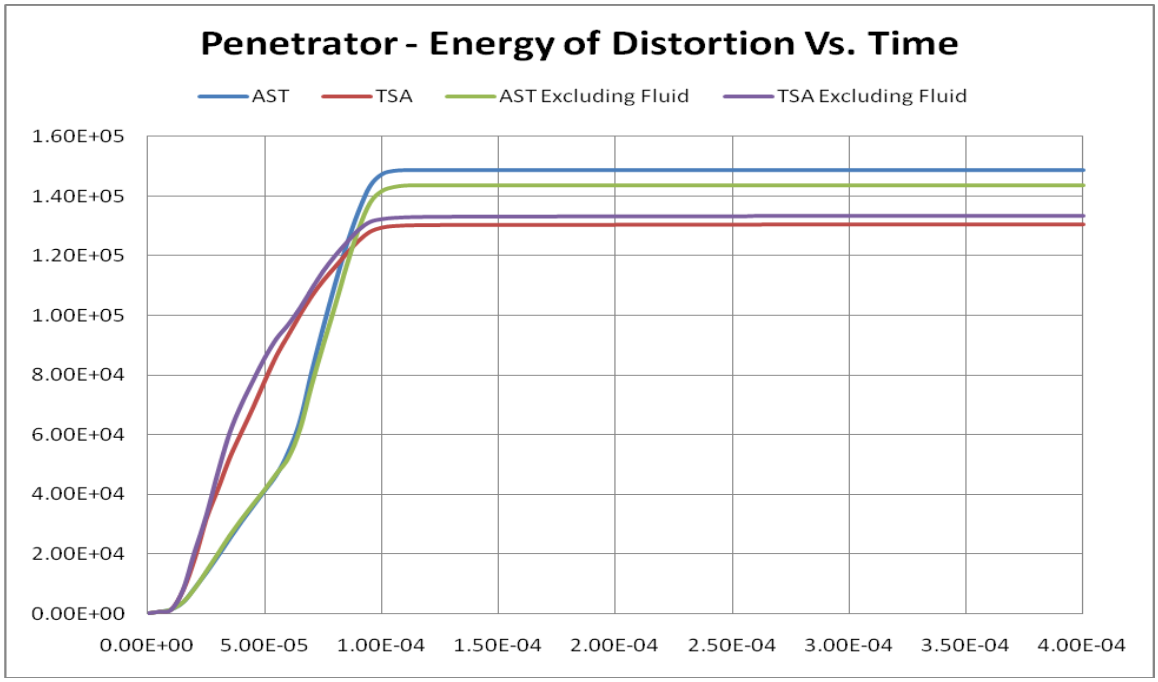

Figure 38: Penetrator Energy of Distortion vs. Time

The internal energy for a material is the sum of the internal energy of all the elements that are in that material. The internal energy for one element is defined

as the sum (in time) of the total stresses multiplied by the strain increments multiplied by the change in time [18]. Figure 39 and Figure 40 show the Internal Energy vs. Time plot of each material for both penetrator configurations.

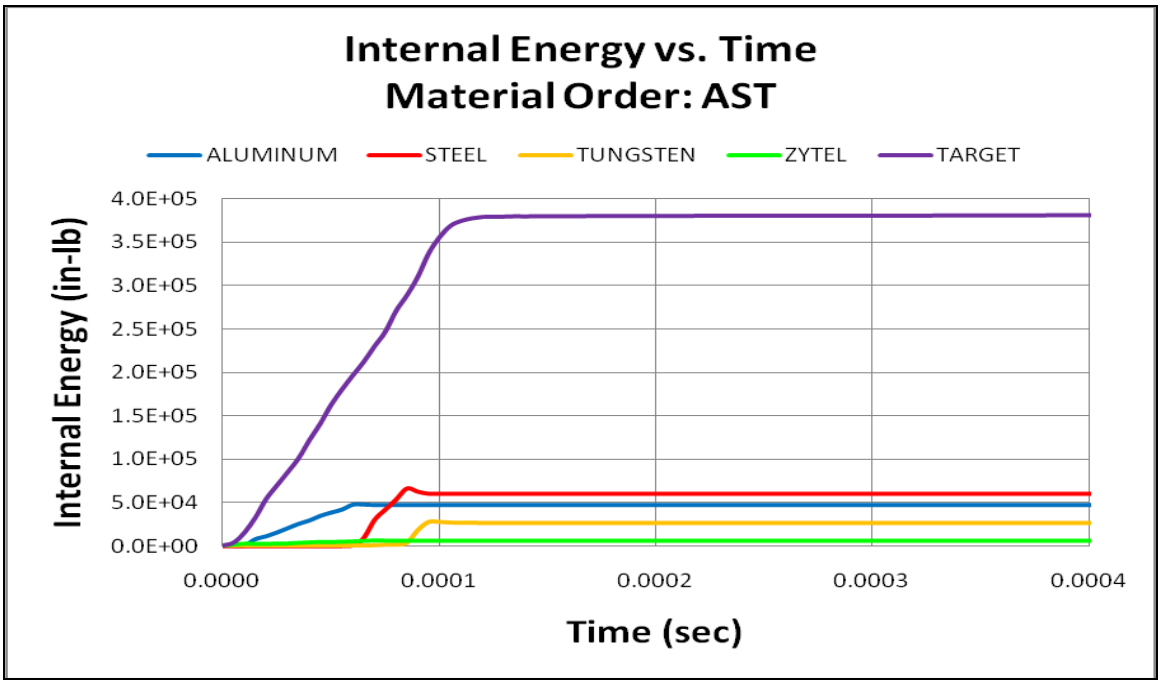

Figure 39: AST Internal Energy vs. Time

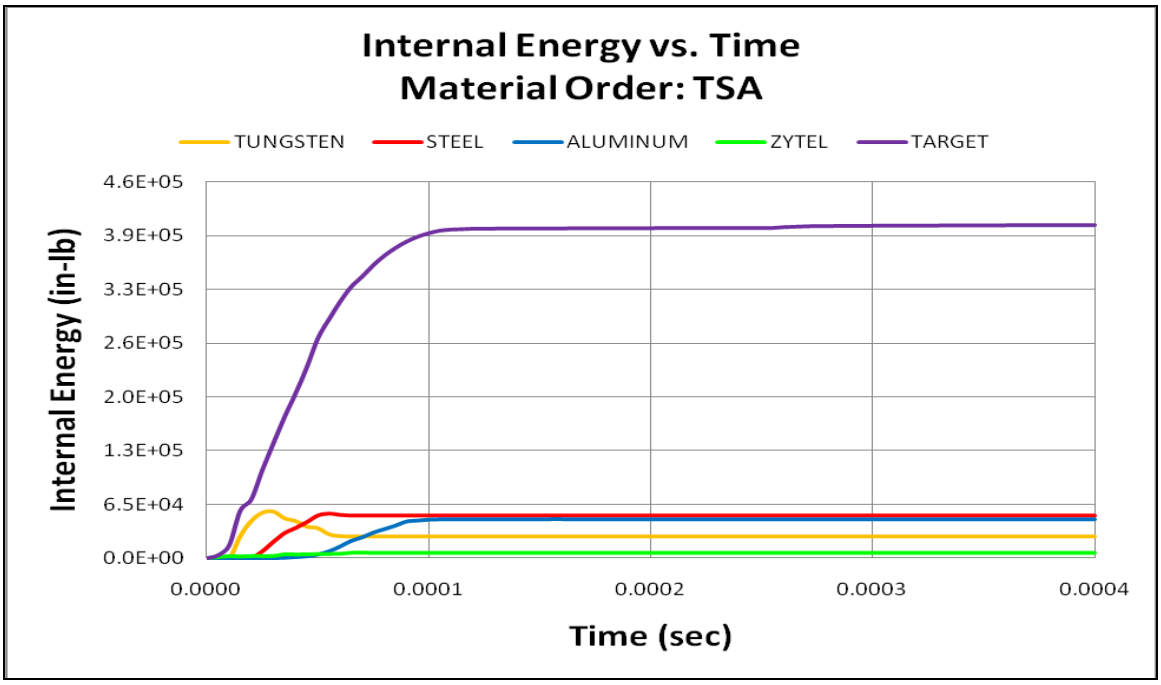

Figure 40: TSA Internal Energy vs. Time

For ease of comparison the internal energy curves for both configurations are given in the following plots. Figure 41 shows the internal energy of the target. Figure 42 shows the internal energy of the complete penetrator. This as with the distortional energy comparison charts given previously is calculated by summing the internal energy for the tungsten, steel, aluminum, and zytel sections. It can be seen from these figures that the target incurs a larger internal energy when the penetrator is in the TSA configuration, but the penetrator incurs a larger internal energy when it is in the AST configuration.

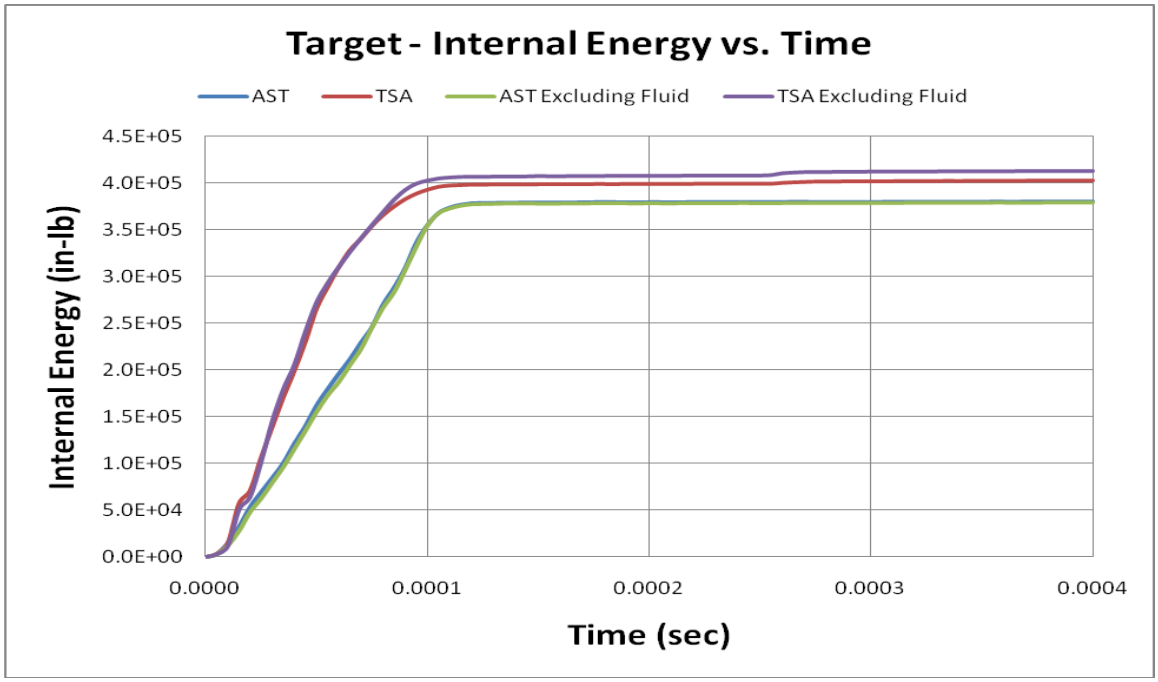

Figure 41: Target Internal Energy vs. Time

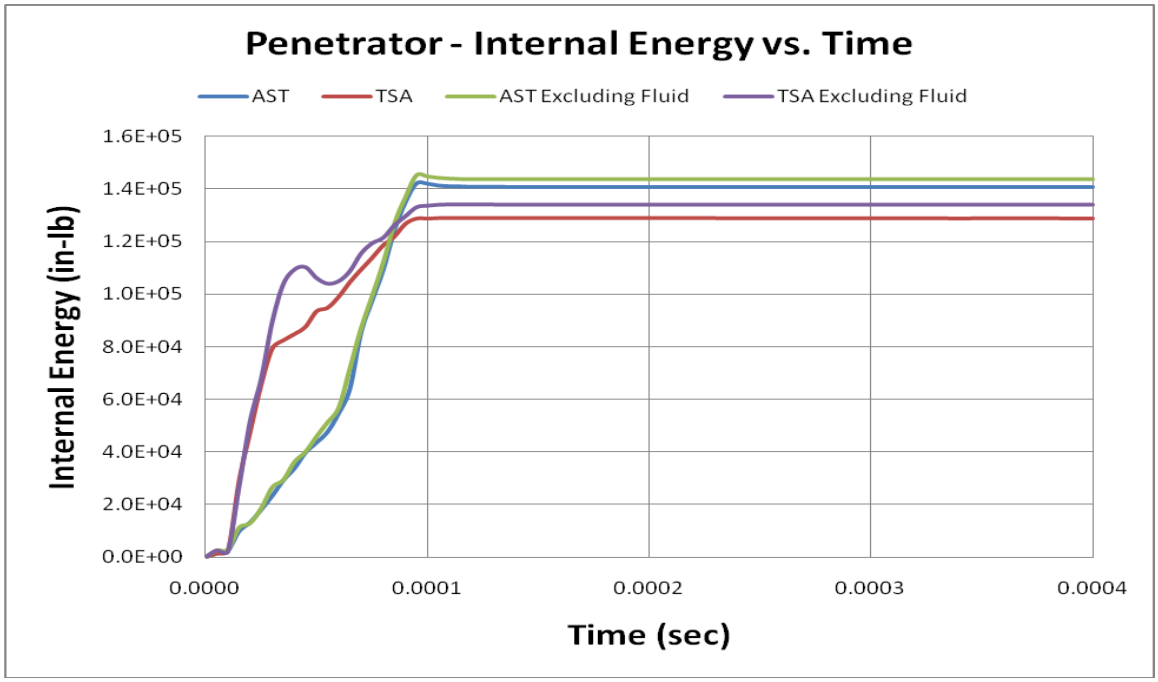

Figure 42: Penetrator Internal Energy vs. Time

The kinetic energy time versus time plots of each solid material are given for both penetrator configurations in Figure 43 and Figure 44.

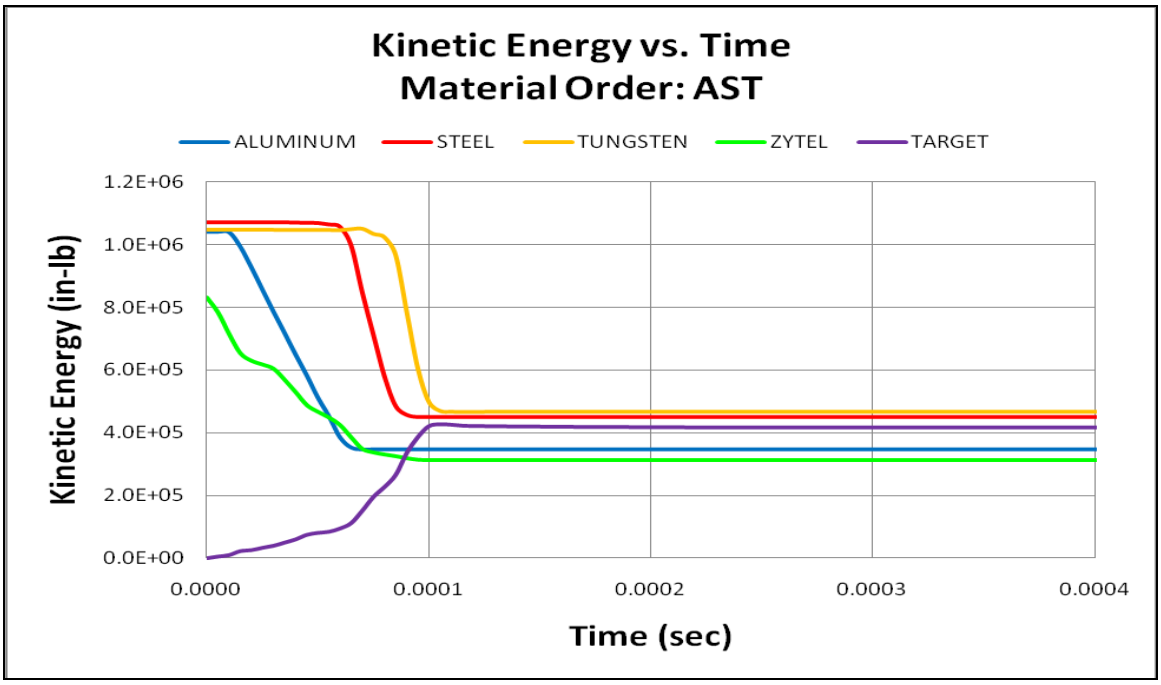

Figure 43: AST Kinetic Energy vs. Time

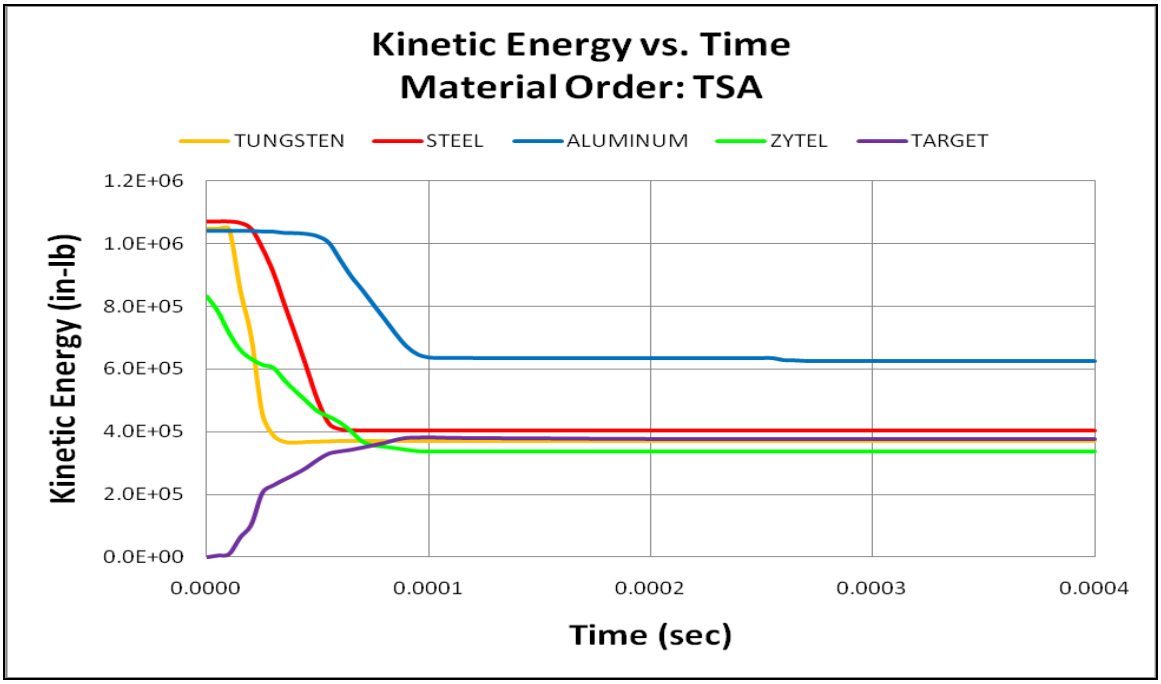

Figure 44: TSA Kinetic Energy vs. Time

It is shown in Figure 45 that the kinetic energy gain in the target occurs substantially quicker when impacted with the TSA configuration penetrator, but

the AST configuration penetrator imparts more kinetic energy to the target as seen by the higher peak in the AST curve. It is also shown in this figure that the difference in the kinetic energy of the target when the fluid is included is substantial. Figure 46 shows the kinetic energy versus time for each penetrator configuration. The TSA configuration's loss of kinetic energy occurs much quicker than the AST configuration, but the AST configuration has a higher total loss of kinetic energy. This is as we would expect after seeing the quicker gain of the TSA configuration and the higher peak of the AST configuration in the target kinetic energy comparison chart.

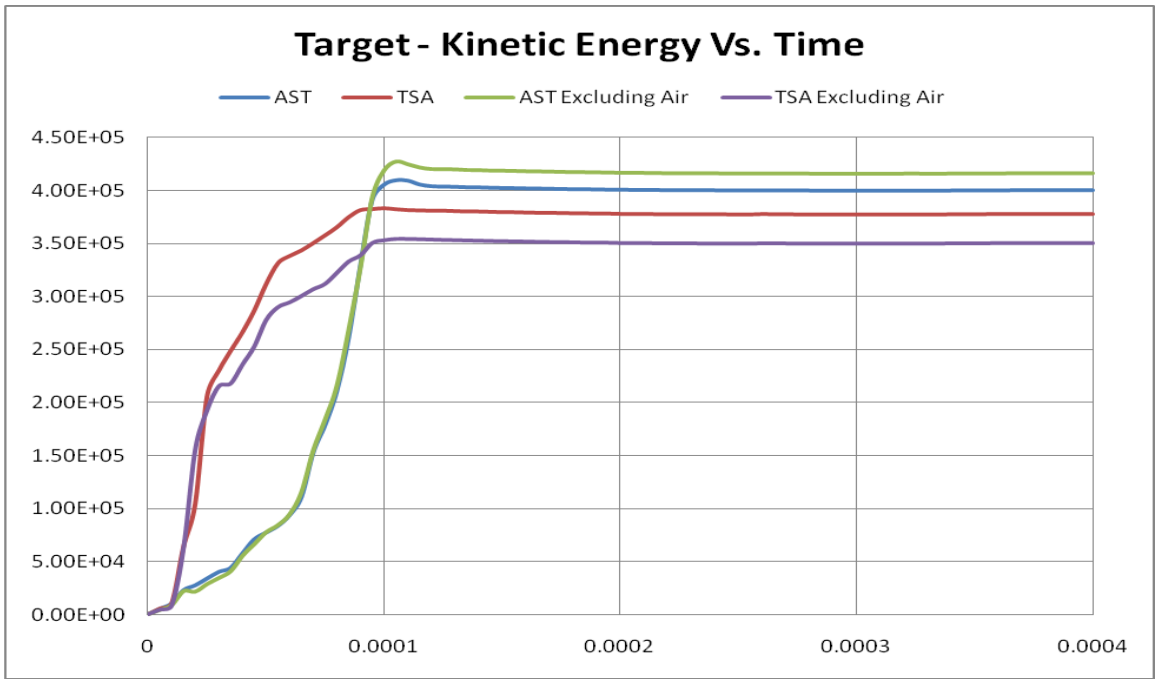

Figure 45: Target Kinetic Energy vs. Time

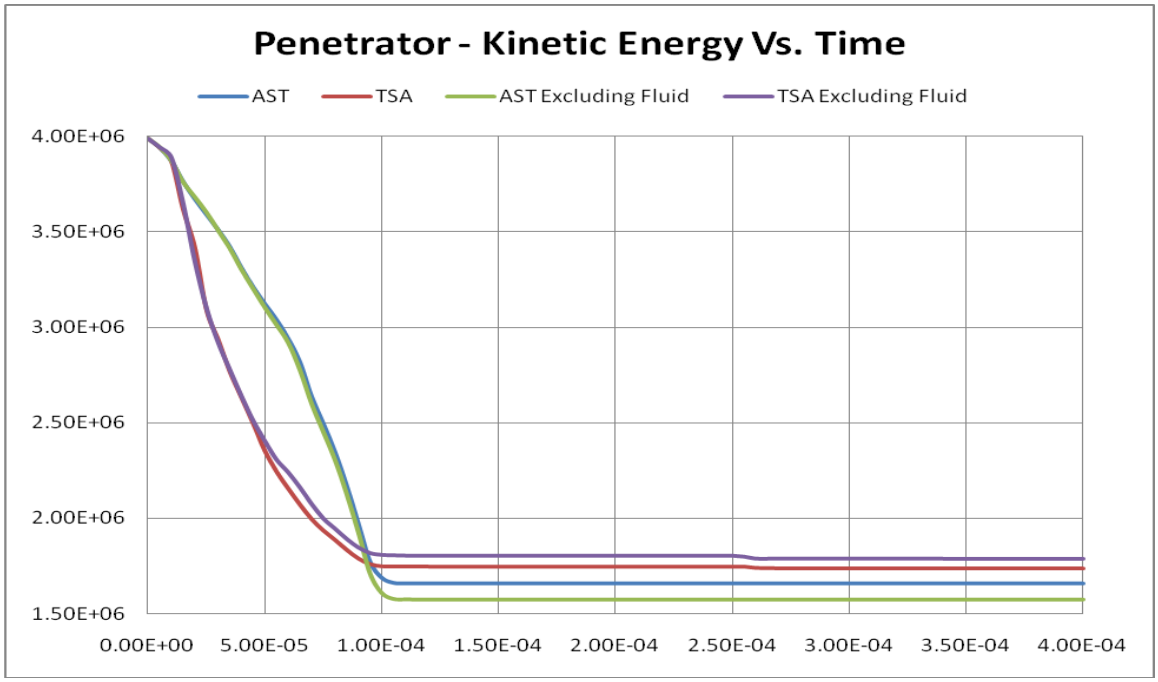

Figure 46: Penetrator Kinetic Energy vs. Time

The plots showing the X, Y, and Z momentum versus time are given in Figure 47 through Figure 52. It is shown that the momentum profiles are similar between the two penetrator configurations and the largest momentum occurs in the Z direction as expected since this is the penetrator's direction of travel.

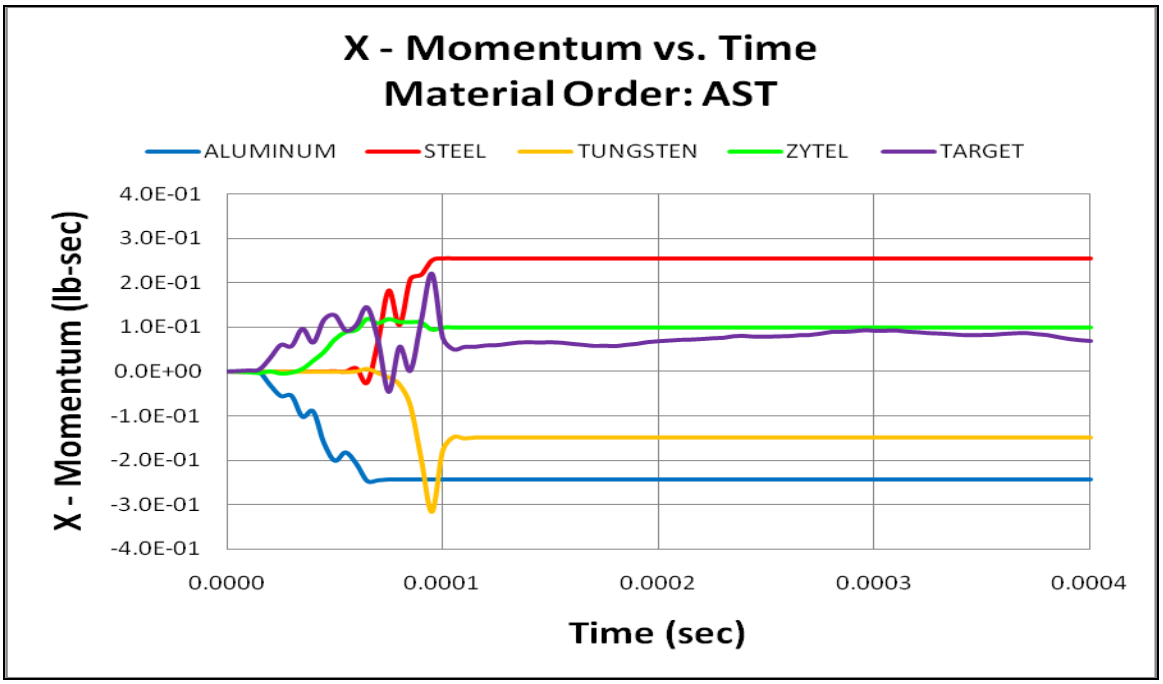

Figure 47: AST X - Momentum vs. Time

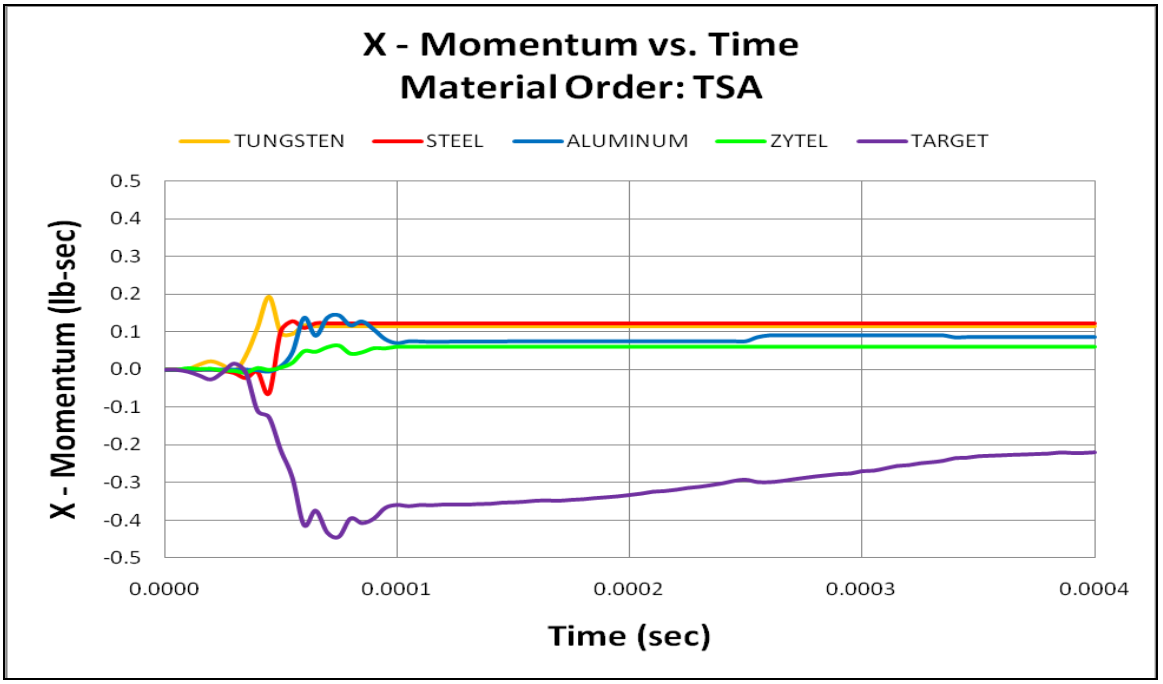

Figure 48: TSA X - Momentum vs. Time

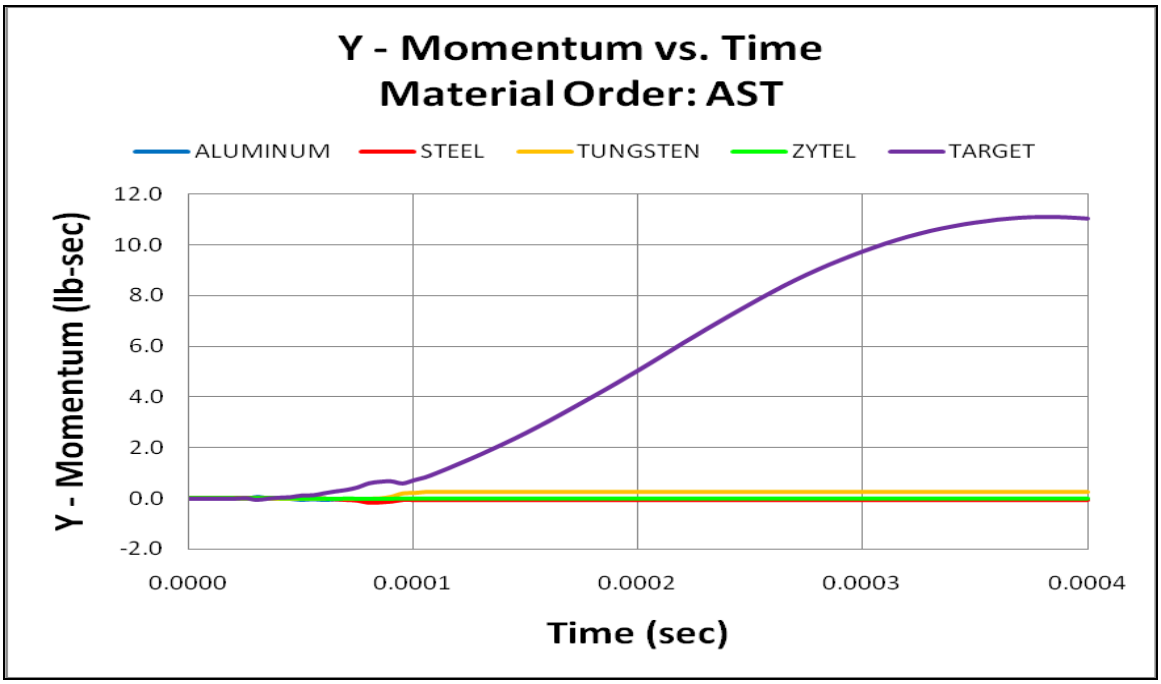

Figure 49: AST Y - Momentum vs. Time

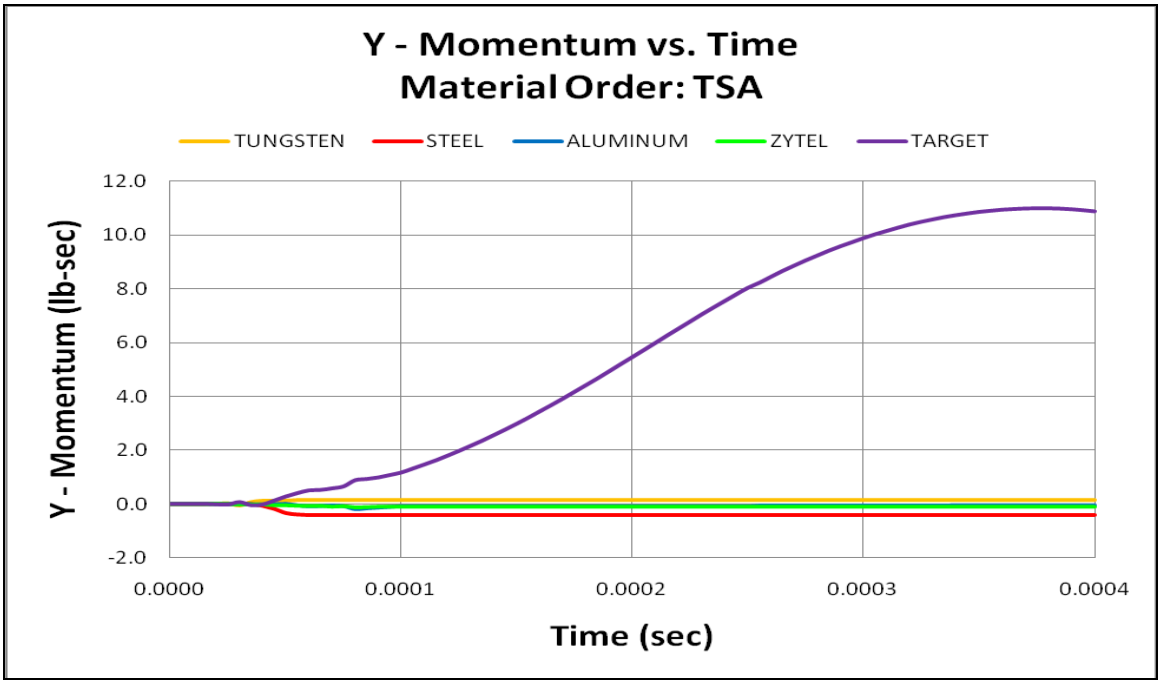

Figure 50: TSA Y - Momentum vs. Time

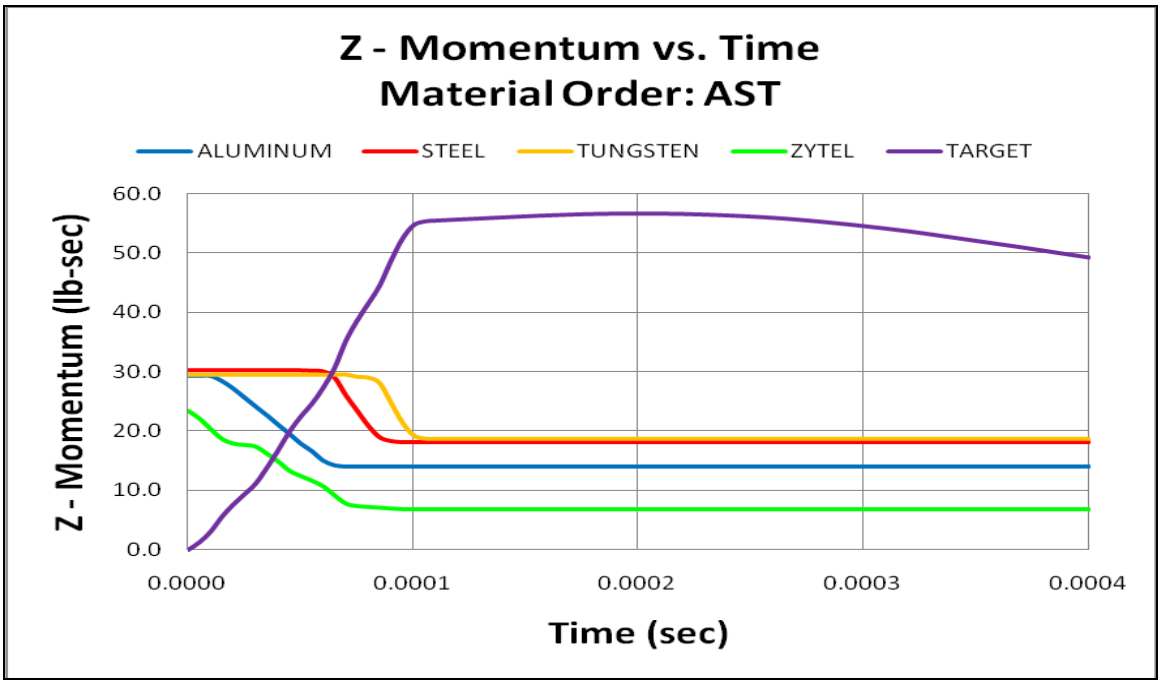

Figure 51: AST Z - Momentum vs. Time

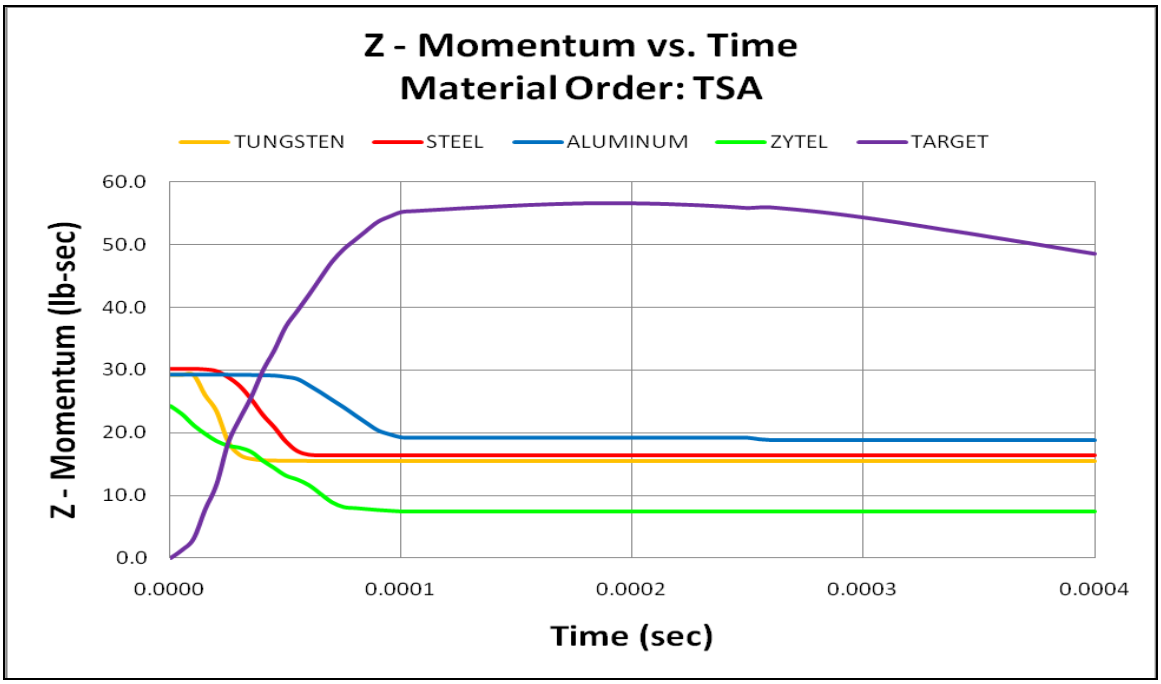

Figure 52: TSA Z - Momentum vs. Time

The second set of results given is the energy of distortion contour plots of the penetrator for both configurations. These plots highlight the energy of distortion

in the metallic rods of the penetrator at select time steps. The failed elements were excluded from the result which allows visualization of the penetrator disintegration that occurs. The last time step before the AST penetrator is completely disintegrated is 0.00014 second. The plots for both penetrators are given side by side in Figure 53 through Figure 80. The plots are given in time increments of approximately 0.00001 second beginning at the closest time step to 0.00001 second and ending at the closest time step to 0.00014 second. Note the color spectrums on these plots are different scales. The scale also varies with each time step.

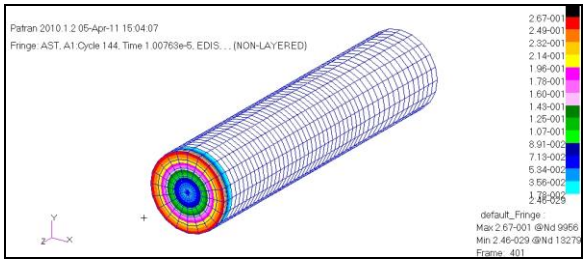

Figure 53: AST Penetrator, 1.0e-5 sec.

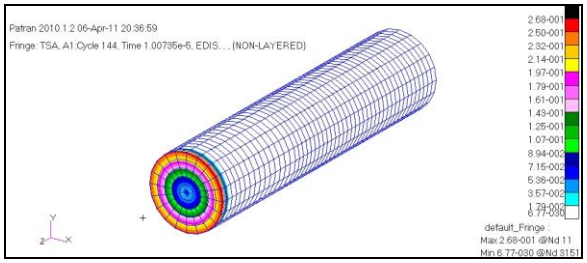

Figure 54: TSA Penetrator, 1.0e-5 sec.

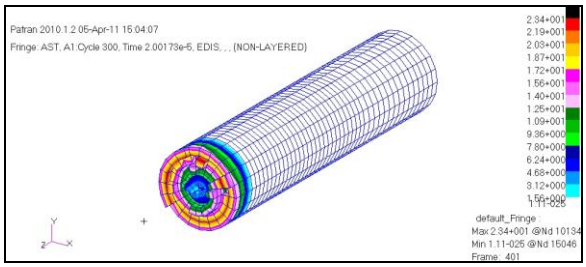

Figure 55: AST Penetrator, 2.0e-5 sec.

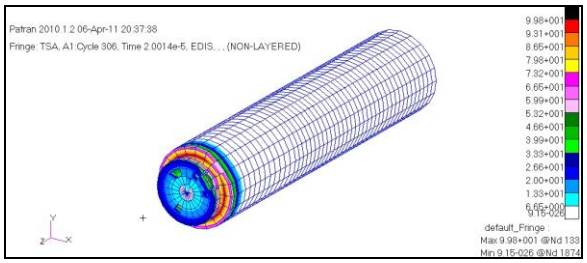

Figure 56: TSA Penetrator, 2.0e-5 sec.

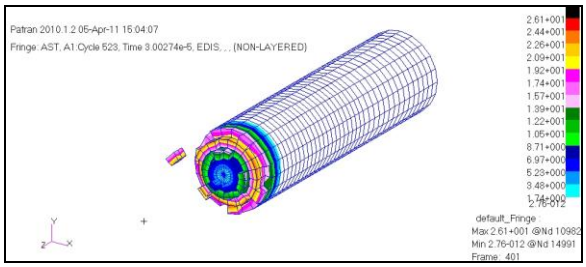

Figure 57: AST Penetrator, 3.0e-5 sec.

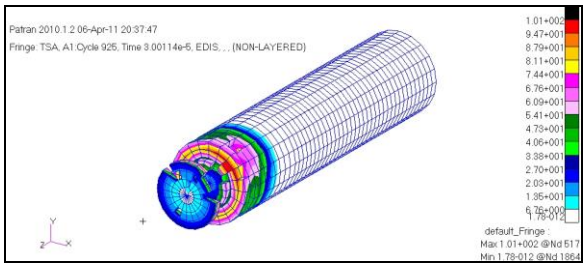

Figure 58: TSA Penetrator, 3.0e-5 sec.

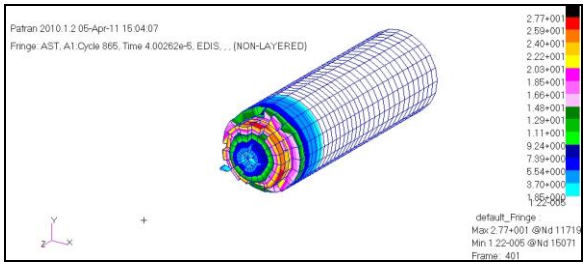

Figure 59: AST Penetrator, 4.0e-5 sec.

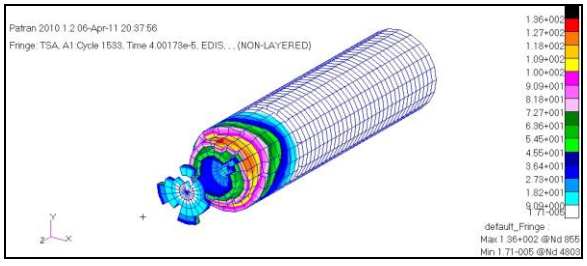

Figure 60: TSA Penetrator, 4.0e-5 sec.

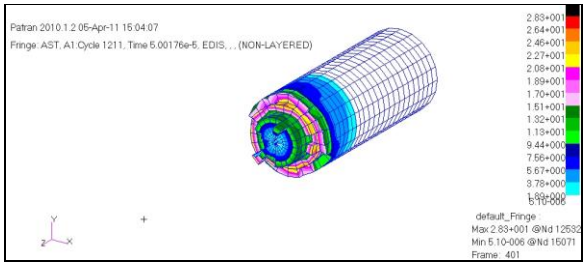

Figure 61: AST Penetrator, 5.0e-5 sec.

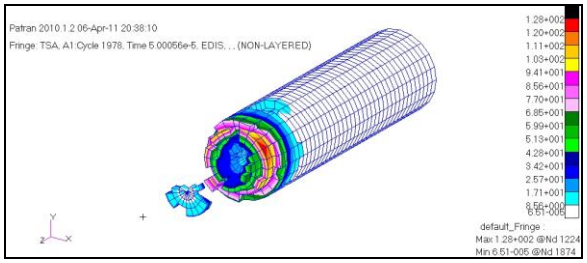

Figure 62: TSA Penetrator, 5.0e-5 sec.

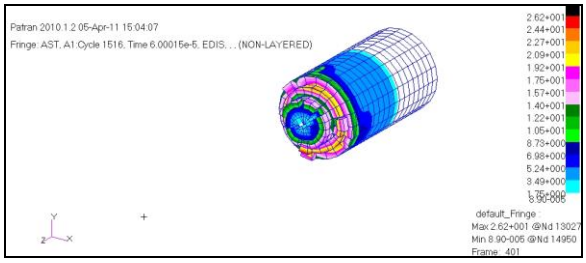

Figure 63: AST Penetrator, 6.0e-5 sec.

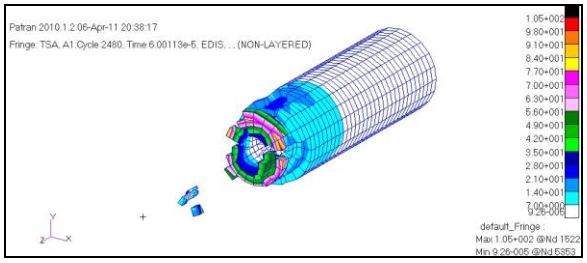

Figure 64: TSA Penetrator, 6.0e-5 sec.

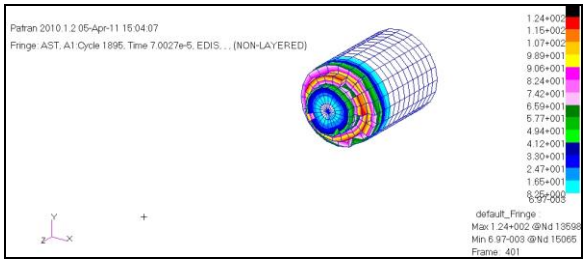

Figure 65: AST Penetrator, 7.0e-5 sec.

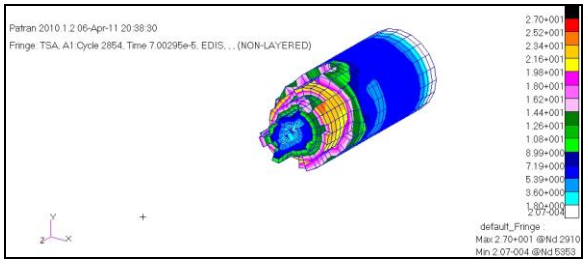

Figure 66: TSA Penetrator, 7.0e-5 sec.

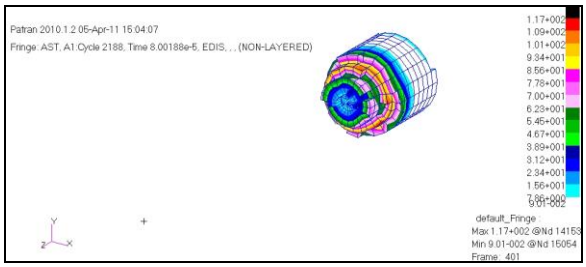

Figure 67: AST Penetrator, 8.0e-5 sec.

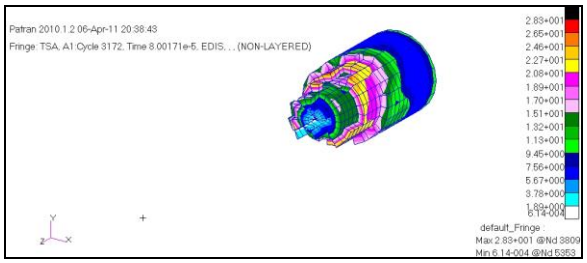

Figure 68: TSA Penetrator, 8.0e-5 sec.

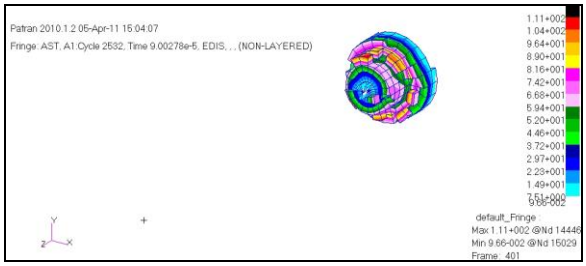

Figure 69: AST Penetrator, 9.0e-5 sec.

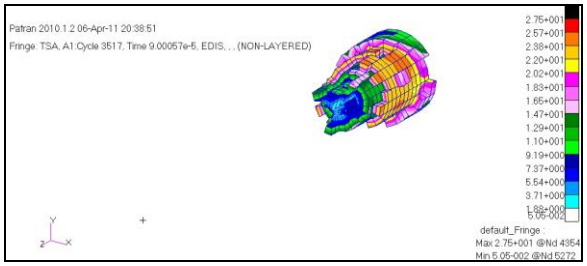

Figure 70: TSA Penetrator, 9.0e-5 sec.

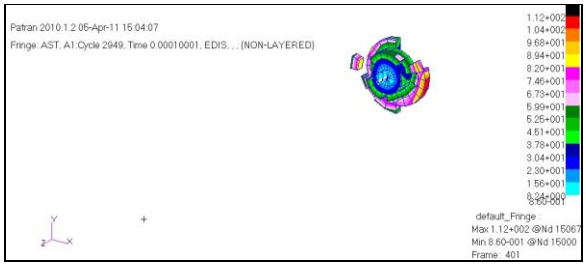

Figure 71: AST Penetrator, 1.0e-4 sec.

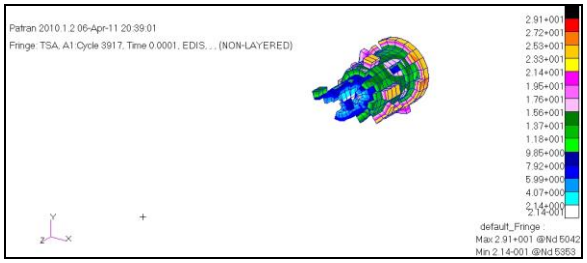

Figure 72: TSA Penetrator, 1.0e-4 sec.

Figure 73: AST Penetrator, 1.1e-4 sec.

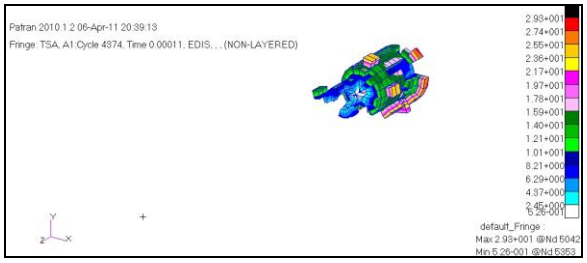

Figure 74: TSA Penetrator, 1.1e-4 sec.

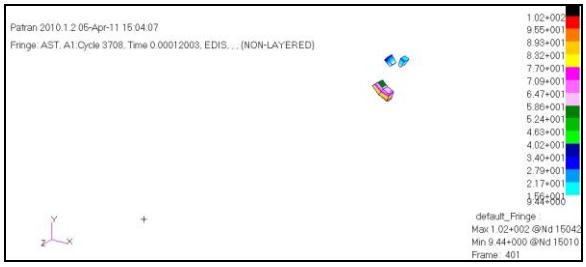

Figure 75: AST Penetrator, 1.2e-4 sec.

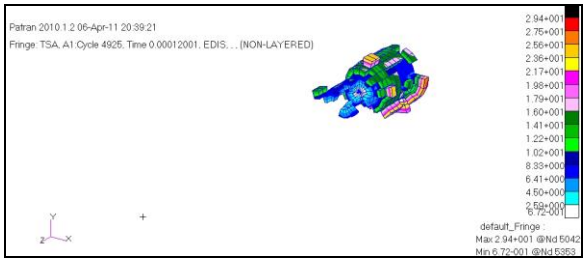

Figure 76: TSA Penetrator, 1.2e-4 sec.

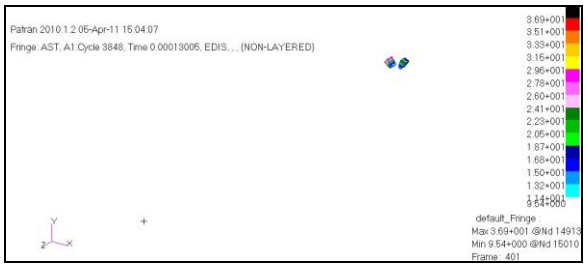

Figure 77: AST Penetrator, 1.3e-4 sec.

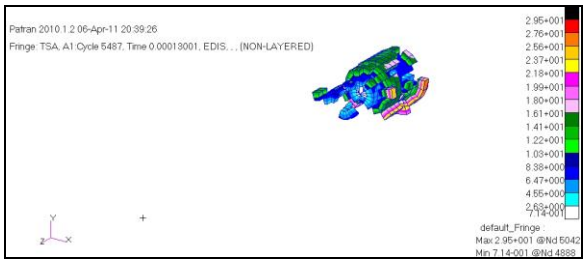

Figure 78: TSA Penetrator, 1.3e-5 sec.

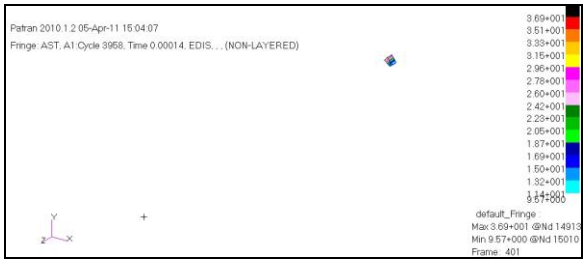

Figure 79: AST Penetrator, 1.4e-4 sec.

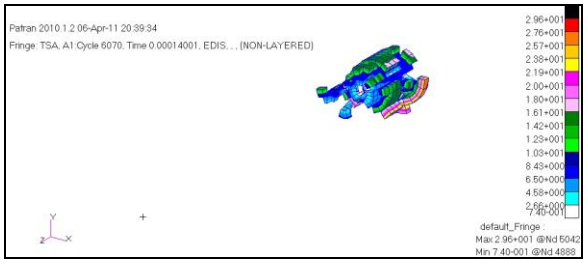

Figure 80: TSA Penetrator, 1.4e-4 sec.

The front plate displacement plots for both configurations are given in the figures below with time increments of 0.00001 second beginning at 0.00001 second and ending at 0.00012 second (time at which AST configuration completely penetrated). The failed elements are removed in order to show the penetration of the front plate. Note the color spectrums on these plots are different scales. The scale also varies with each time step.

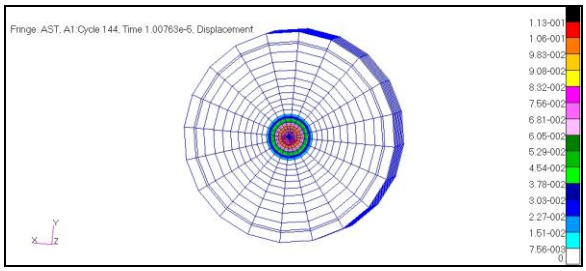

Figure 81: AST Front Plate Displacement, 1.0e-5 sec.

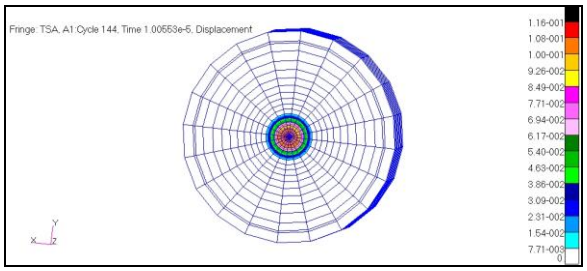

Figure 82: TSA Front Plate Displacement, 1.0e-5 sec.

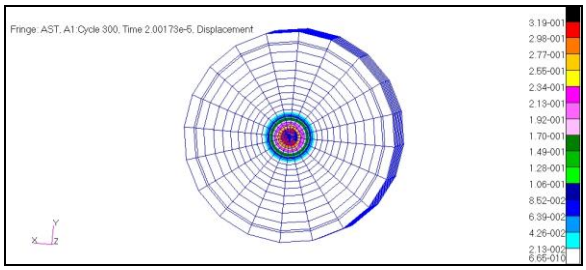

Figure 83: AST Front Plate Displacement, 2.0e-5 sec.

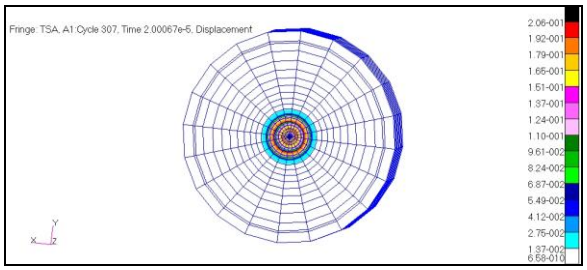

Figure 84: TSA Front Plate Displacement, 2.0e-5 sec.

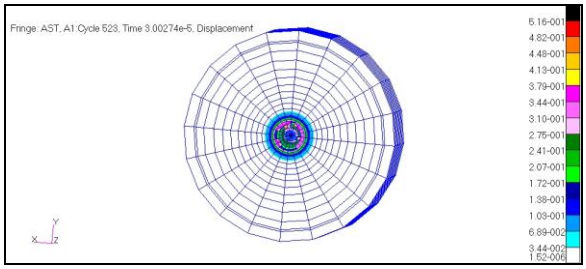

Figure 85: AST Front Plate Displacement, 3.0e-5 sec.

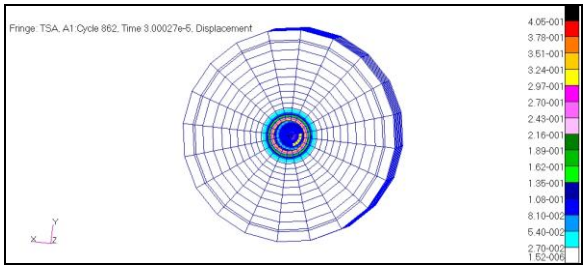

Figure 86: TSA Front Plate Displacement, 3.0e-5 sec.

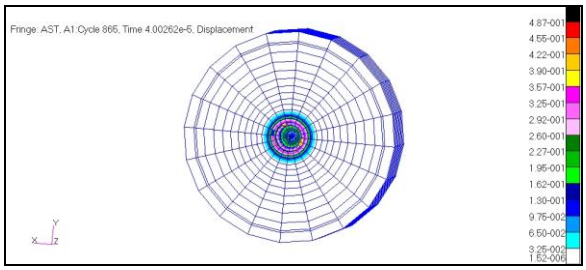

Figure 87: AST Front Plate Displacement, 4.0e-5 sec.

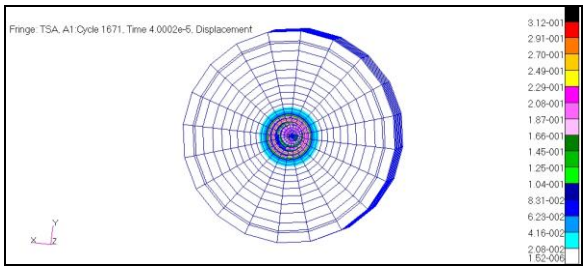

Figure 88: TSA Front Plate Displacement, 4.0e-5 sec.

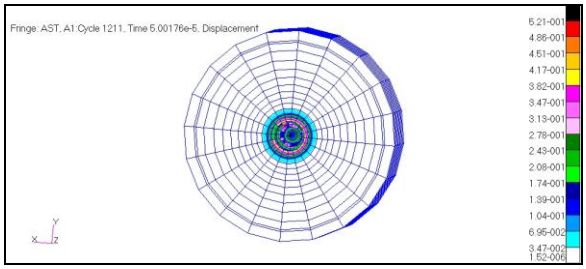

Figure 89: AST Front Plate Displacement, 5.0e-5 sec.

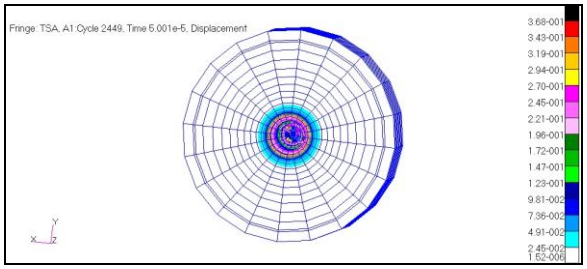

Figure 90: TSA Front Plate Displacement, 5.0e-5 sec.

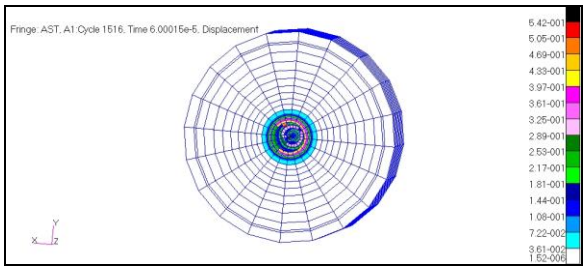

Figure 91: AST Front Plate Displacement, 6.0e-5 sec.

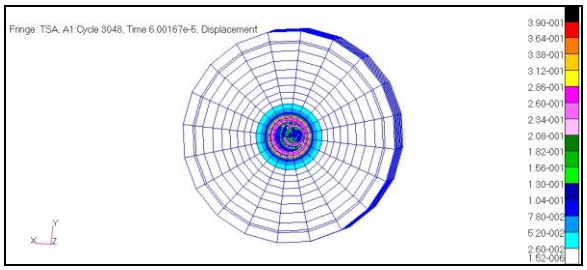

Figure 92: TSA Front Plate Displacement, 6.0e-5 sec.

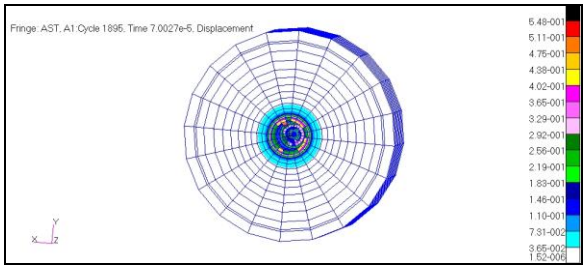

Figure 93: AST Front Plate Displacement, 7.0e-5 sec.

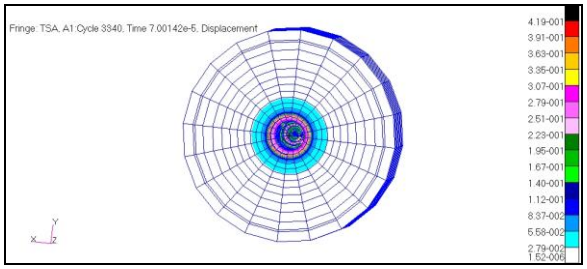

Figure 94: TSA Front Plate Displacement, 7.0e-5 sec.

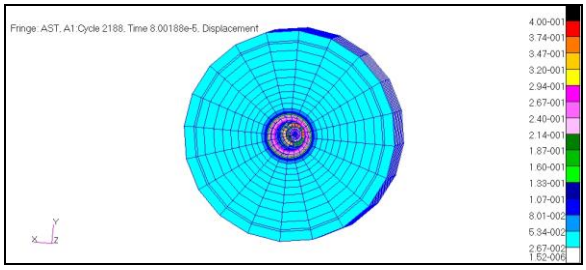

Figure 95: AST Front Plate Displacement, 8.0e-5 sec.

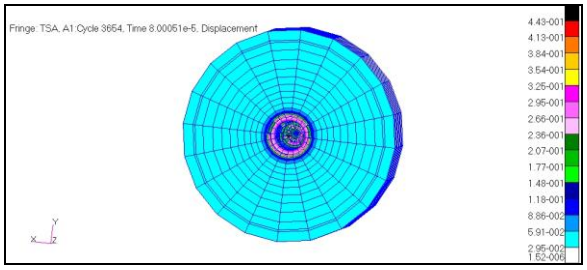

Figure 96: TSA Front Plate Displacement, 8.0e-5 sec.

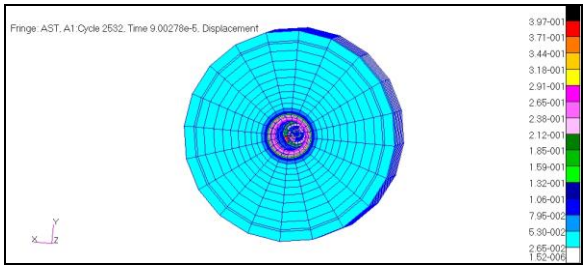

Figure 97: AST Front Plate Displacement, 9.0e-5 sec.

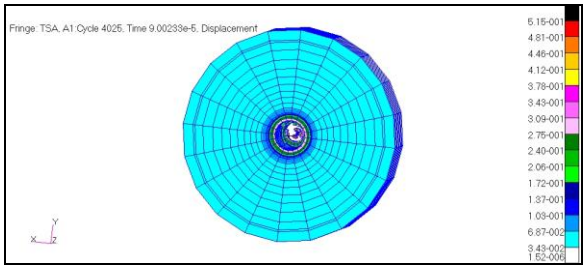

Figure 98: TSA Front Plate Displacement, 9.0e-5 sec.

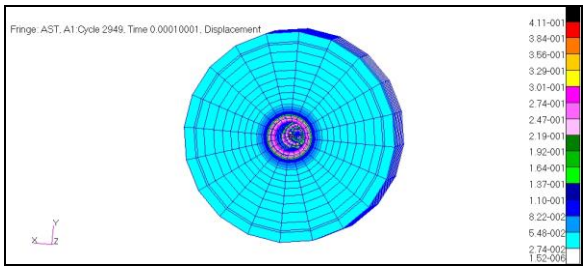

Figure 99: AST Front Plate Displacement, 1.0e-4 sec.

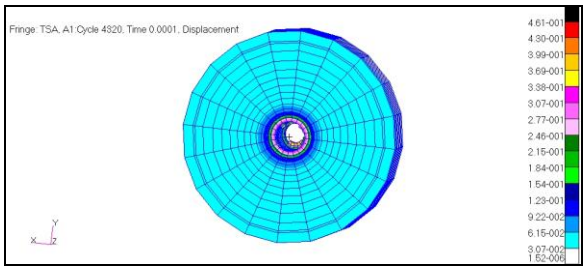

Figure 100: TSA Front Plate Displacement, 1.0e-4 sec.

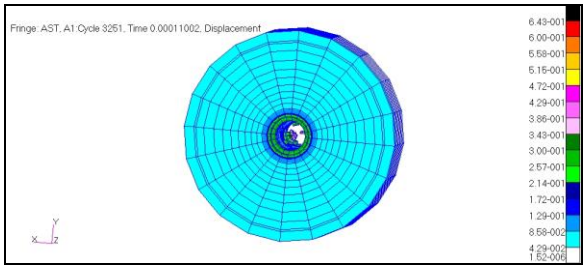

Figure 101: AST Front Plate Displacement, 1.1e-4 sec.

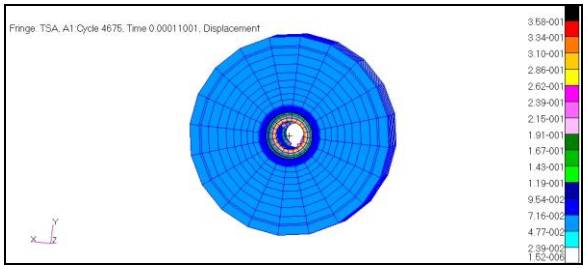

Figure 102: TSA Front Plate Displacement, 1.1e-4 sec.

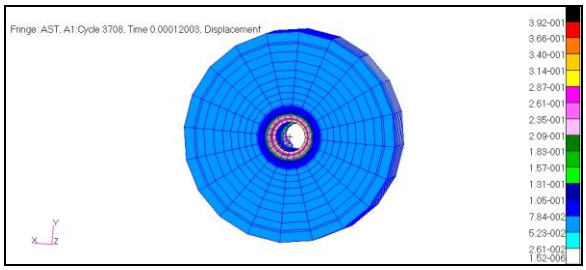

Figure 103: AST Front Plate Displacement, 1.2e-4 sec.

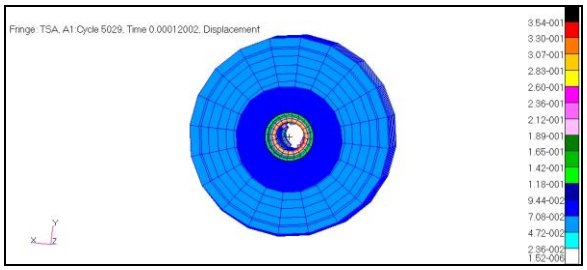

Figure 104: TSA Front Plate Displacement, 1.2e-4 sec.

The final result sets given for the Lagrangian elements will be contours plots of the stress wave as it travels through the front plate, rear plate, and inside walls. The plots for both configurations will be presented at an initial time of approximately 0.00001 second with an increment of 0.00005 second. The last time step given will be approximately 0.00041 second. These plots are shown side by side for easy comparison in Figure 105 through Figure 122. Note the

color spectrums on these plots are different scales. The scale also varies with each time step.

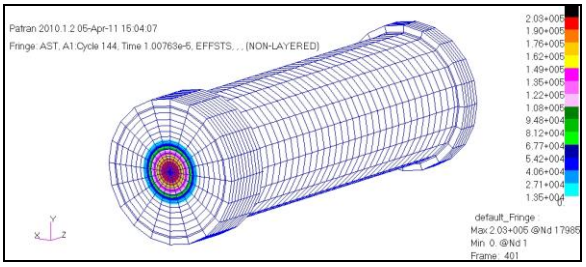

Figure 105: AST Stress, 1.0e-5 sec.

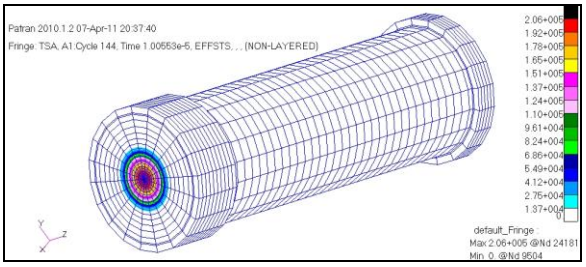

Figure 106: TSA Stress, 1.0e-5 sec.

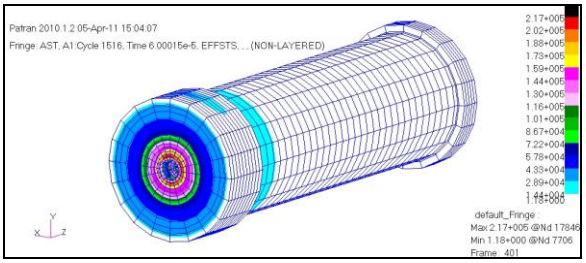

Figure 107: AST Stress, 6.0e-5 sec.

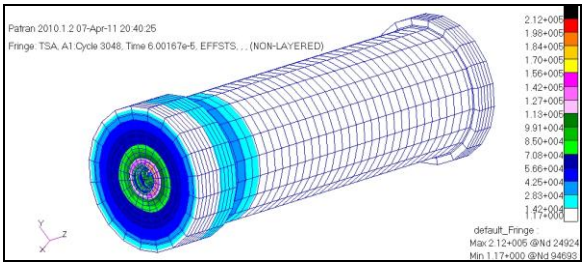

Figure 108: TSA Stress, 6.0e-5 sec.

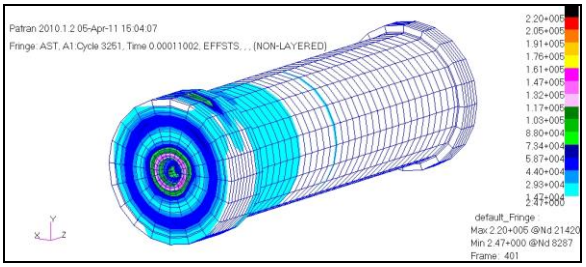

Figure 109: AST Stress, 1.1e-4 sec.

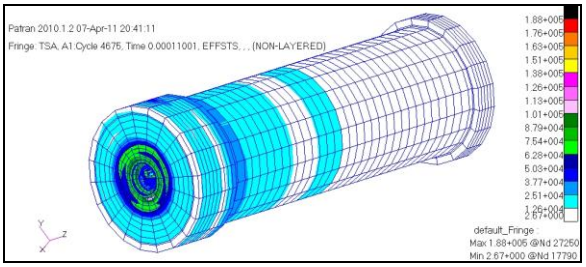

Figure 110: TSA Stress, 1.1e-4 sec.

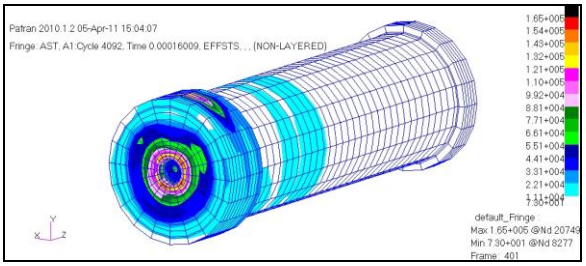

Figure 111: AST Stress, 1.6e-4 sec.

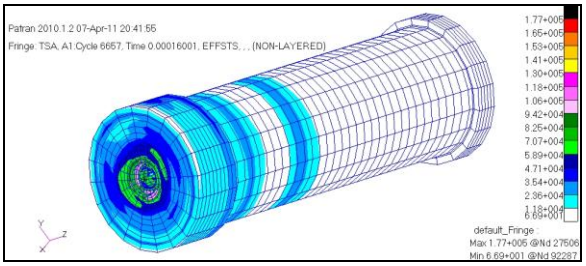

Figure 112: TSA Stress, 1.6e-4 sec.

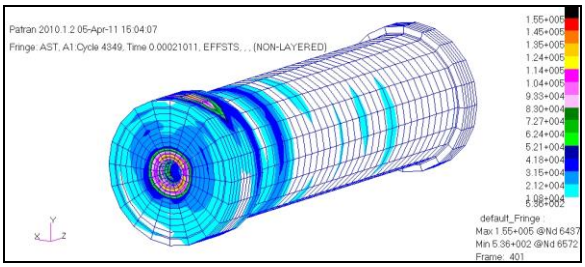

Figure 113: AST Stress, 2.1e-4 sec.

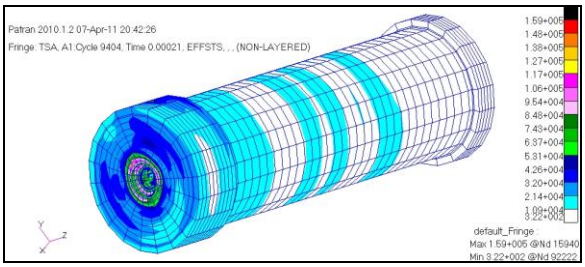

Figure 114: TSA Stress, 2.1e-4 sec.

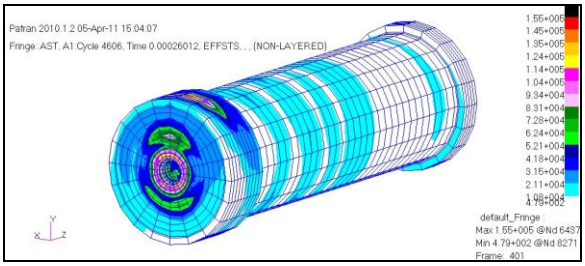

Figure 115: AST Stress, 2.6e-4 sec.

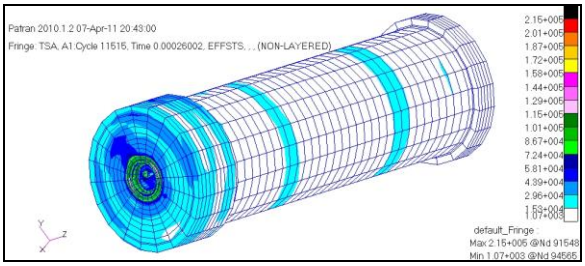

Figure 116: TSA Stress, 2.6e-4 sec.

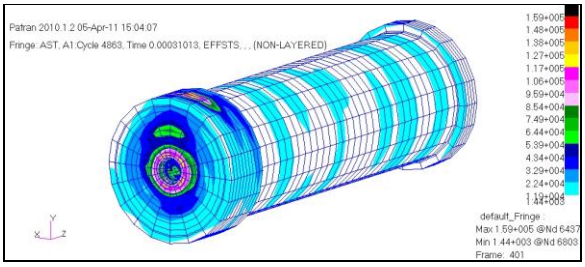

Figure 117: AST Stress, 3.1e-4 sec.

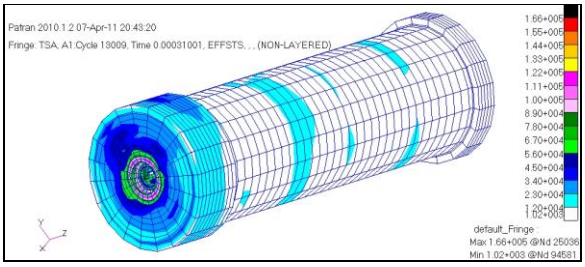

Figure 118: TSA Stress, 3.1e-4 sec.

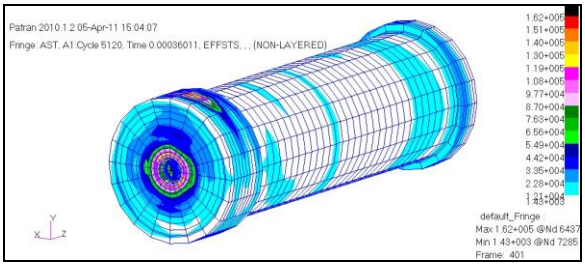

Figure 119: AST Stress, 3.6e-4 sec.

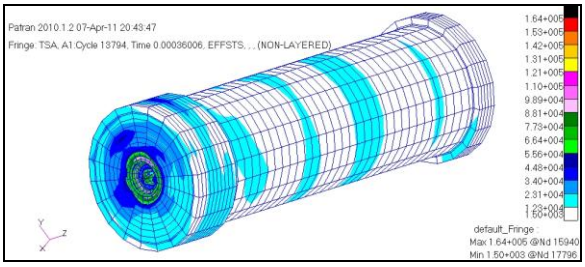

Figure 120: TSA Stress, 3.6e-4 sec.

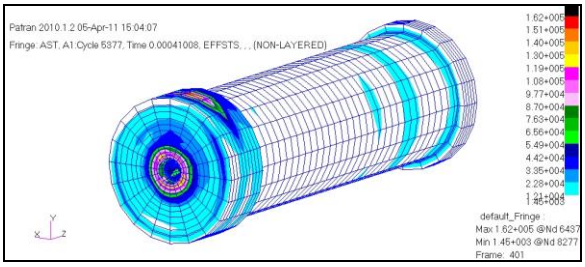

Figure 121: AST Stress, 4.1e-4 sec.

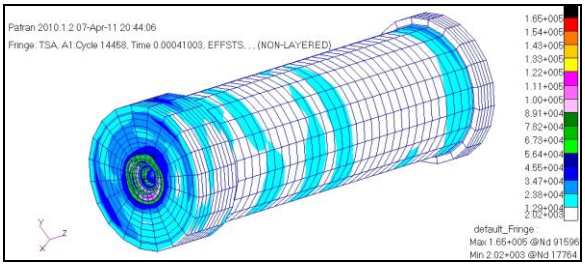

Figure 122: TSA Stress, 4.1e-4 sec.

3.2 Euler

To evaluate the resulting pressure wave that occurs in the interior and on the exterior of the target, plots of the pressure versus Z of the Euler regions for the nodes centered along the X and Y axis as well as contour plots for the faces of select slices of the Euler regions are given for both configurations. Figure 123 shows a pressure wave for the AST configuration as it moves through the first interior Euler region from time 0 to 0.0004 second. Figure 124 shows the corresponding pressure wave for the TSA configuration.

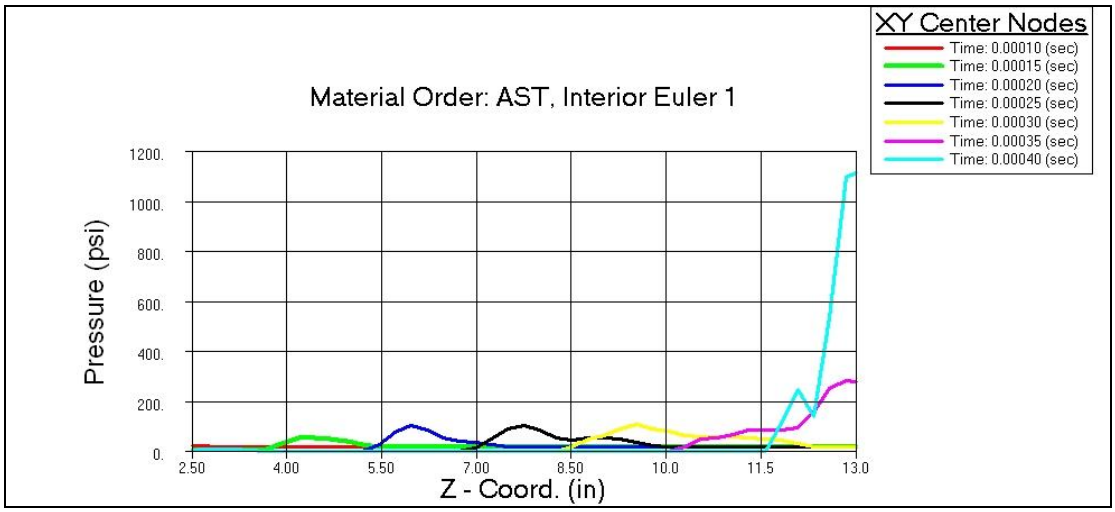

Figure 123: AST Interior Euler 1, Pressure vs. Z-Coord.

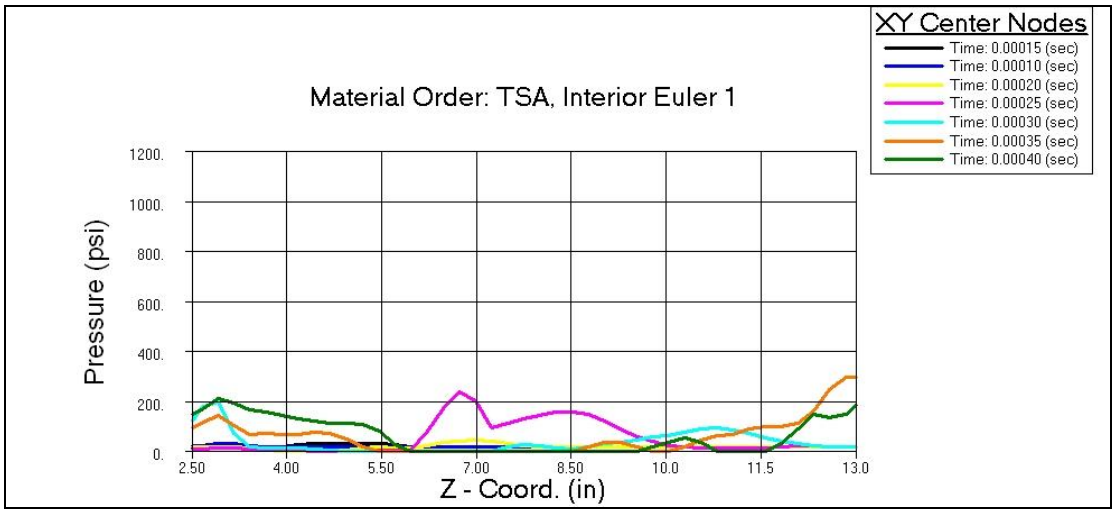

Figure 124: TSA Interior Euler 1, Pressure vs. Z-Coord.

The second AST configuration, interior Euler region had minimal pressure change until approximately 0.0006 second. Due to this Figure 125, which shows the pressures as it fluctuates along the Z-axis at the X and Y-axis centered nodes in this region, begins at 0.0006 second and ends at 0.0010 second. Figure 126 shows the pressure of the second interior Euler region for the TSA configuration.

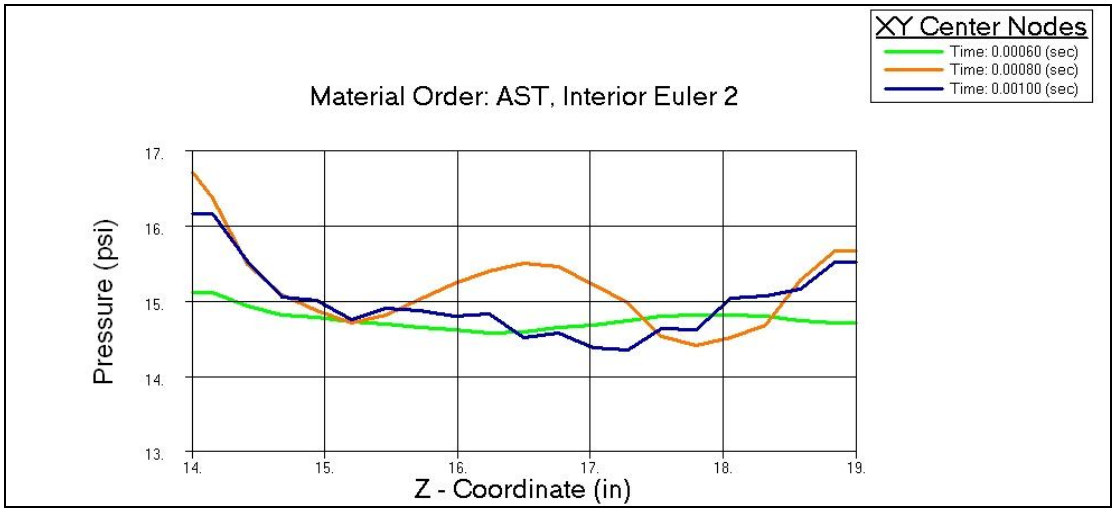

Figure 125: AST Interior Euler 2, Pressure vs. Z-Coord.

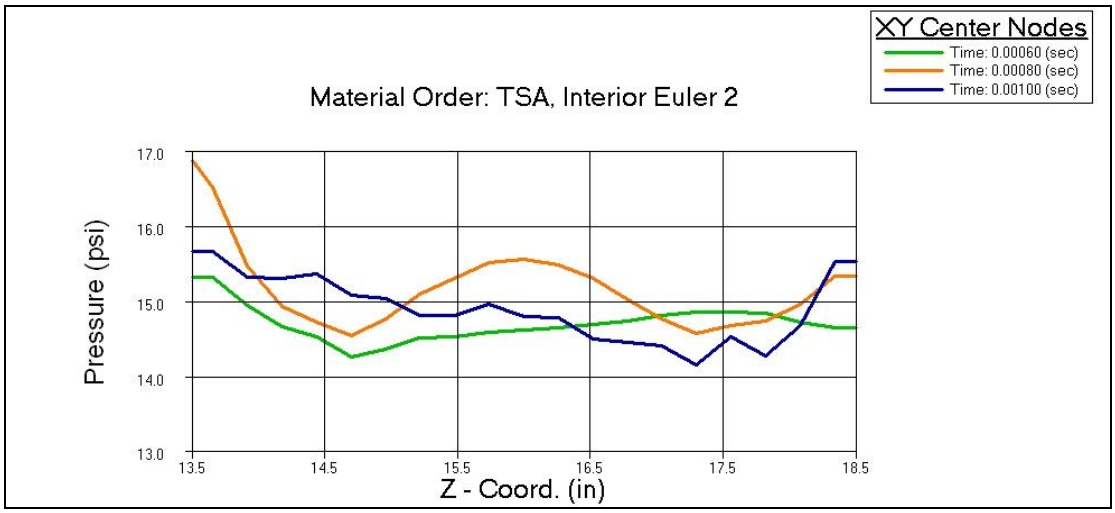

Figure 126: TSA Interior Euler 2, Pressure vs. Z-Coord.

The contour plots for the Euler regions are given next. Before these results are presented the region definitions segmented for viewing the results will be explained. The Euler regions in each of the three compartments (target sections between front plate, bulkheads, and rear plate) are segmented into three slices (Front, Middle, and Back) each. In addition the hole between the two compartments in the first Euler region is given as a separate segment. Figure 127 shows each labeled contour segment in relation to the front plate, rear plate, and solid bulkhead. So the reader may see the section of the target that contains the Euler 1 hole contour segment, Figure 128 shows the first Euler region with the Euler 1 hole contour segment removed.

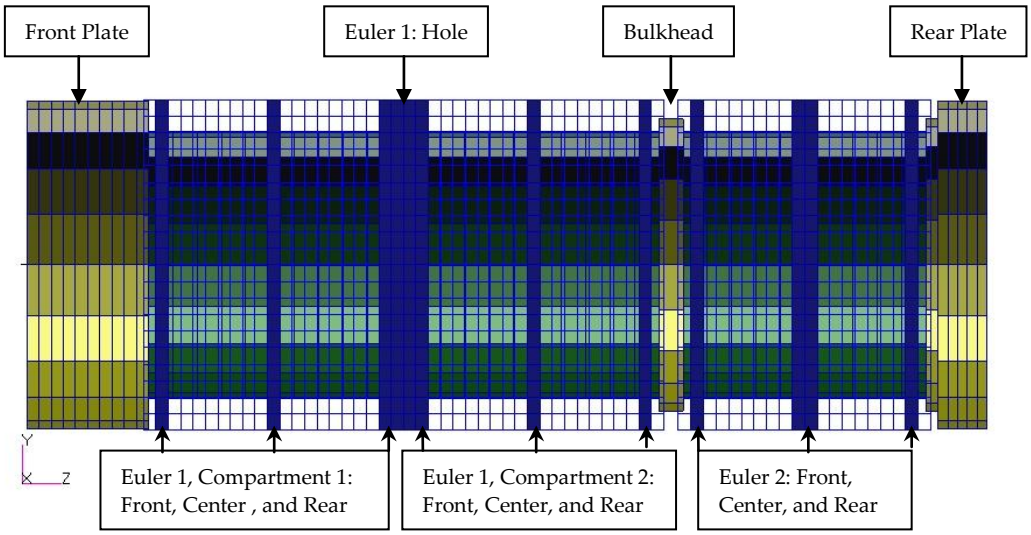

Figure 127: Euler Contour Regions

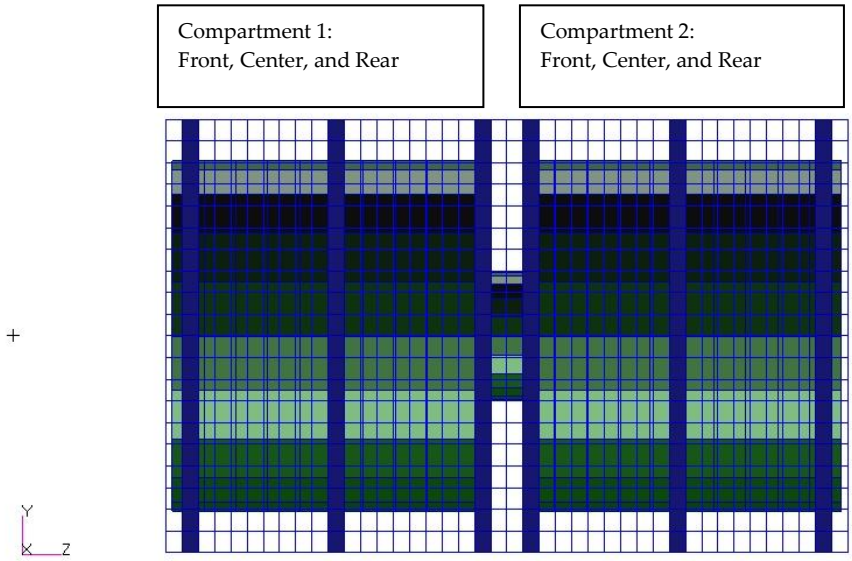

Figure 128: Euler 1 Contour Regions Excluding Hole

The pressure contour plots of the front and center slices of compartment 1, hole slice, and the center and rear slices of compartment 2 from the first interior Euler region given below begins at approximately 0.0001 second, increments approximately 0.00005 second, and ends at approximately 0.0004 second. Figure

129 shows the pressure increase in the front slice of the first Euler region for the AST configuration at 0.0001 second. Figure 130 shows the pressure increase in the front slice of the first Euler region for the TSA configuration at 0.0001 second. The plots for the other 6 time steps are given in Figure 131 through Figure 142. Note the pressure begins to build on the front slice of the TSA configuration at approximately 0.000025 second sooner than on the AST configuration. This is likely due to the TSA configuration penetrating the front plate faster than the AST configuration.

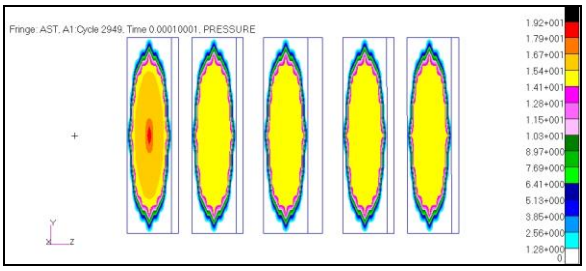

Figure 129: AST Euler Region 1 Pressure, 1e-4 sec.

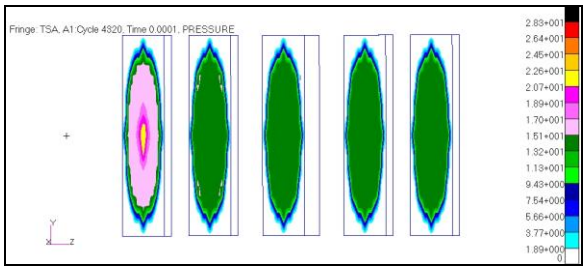

Figure 130: TSA Euler Region 1 Pressure, 1e-4 sec.

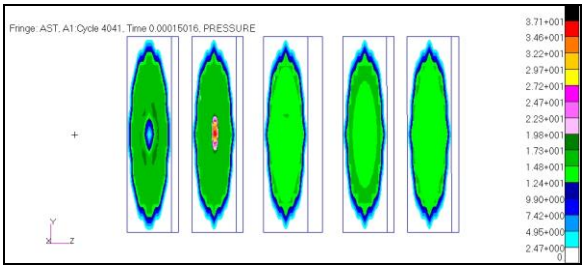

Figure 131: AST Euler Region 1, 1.5e-4 sec.

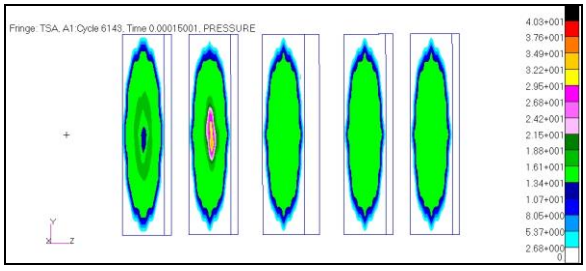

Figure 132: TSA Euler Region 1 Pressure, 1.5e-4 sec.

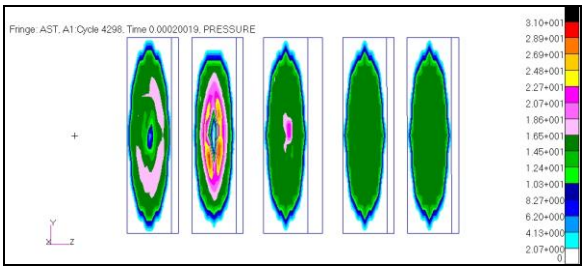

Figure 133: AST Euler Region 1 Pressure, 2.0e-4 sec.

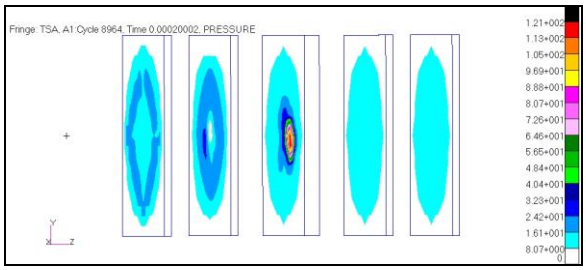

Figure 134: TSA Euler Region 1 Pressure, 2.0e-4 sec.

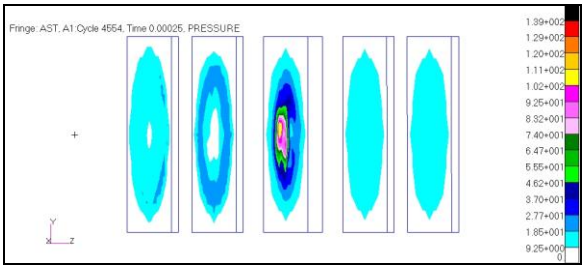

Figure 135: AST Euler Region 1 Pressure, 2.5e-4 sec.

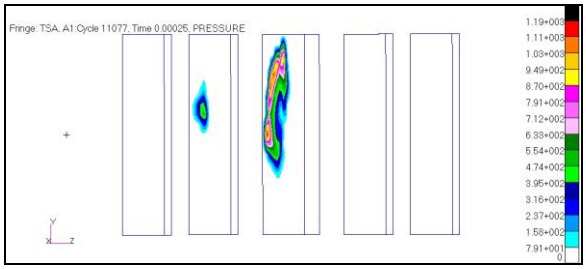

Figure 136: TSA Euler Region 1 Pressure, 2.5e-4 sec.

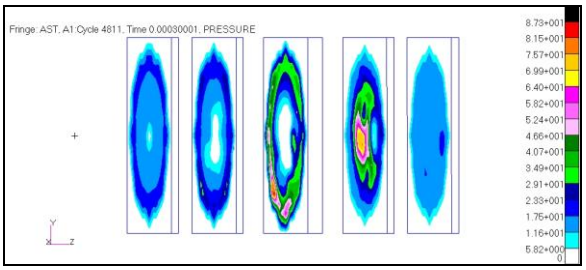

Figure 137: AST Euler Region 1 Pressure, 3.0e-4 sec.

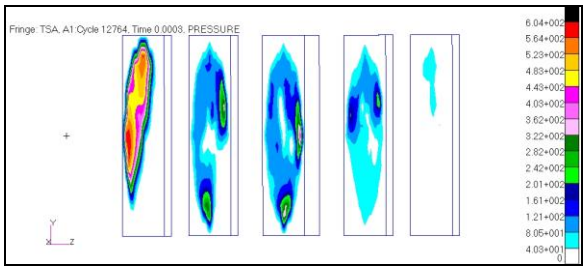

Figure 138: TSA Euler Region 1 Pressure, 3.0e-4 sec.

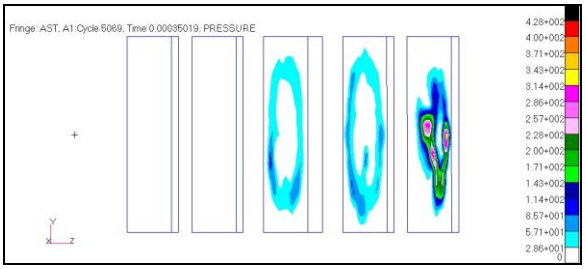

Figure 139: AST Euler Region 1 Pressure, 3.5e-4 sec.

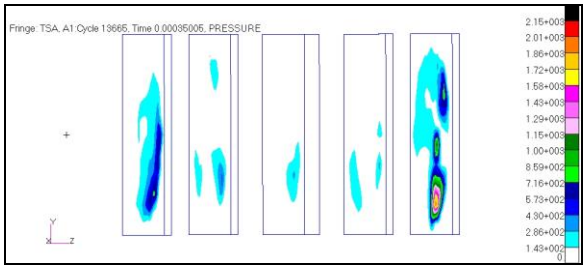

Figure 140: TSA Euler Region 1 Pressure, 3.5e-4 sec.

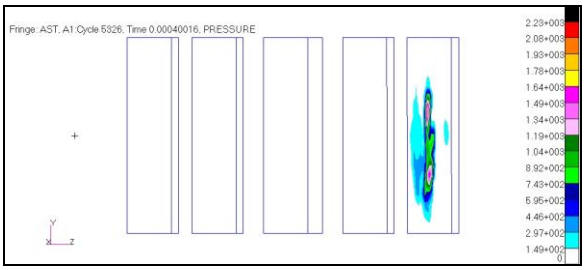

Figure 141: AST Euler Region 1 Pressure, 4.0e-4 sec.

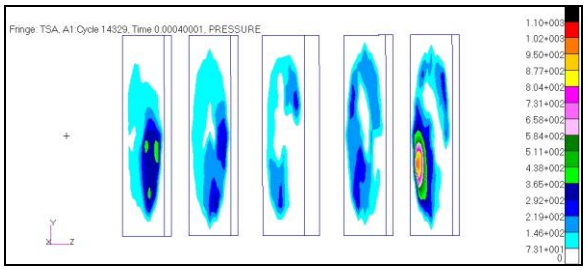

Figure 142: TSA Euler Region 1 Pressure, 4.0e-4 sec.

The pressure contour plots given below of the front, center, and rear slice from the second interior Euler region begins at approximately 0.0008 second, incremented at approximately 0.0001 second, and ends at approximately 0.0011 second. Note the pressures are much less in the second Euler region compared to the first Euler region. This indicates that the solid bulkhead separating the two regions effectively absorbed or reflected the pressure wave.

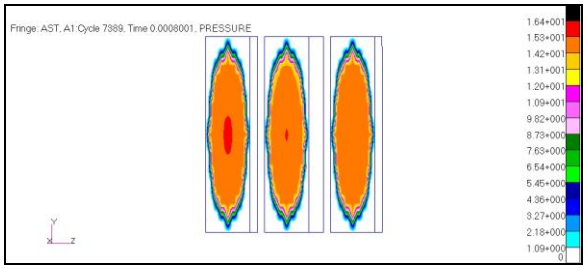

Figure 143: AST Euler Region 2 Pressure, 8e-4 sec.

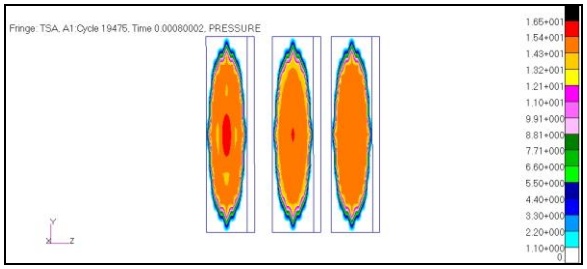

Figure 144: TSA Euler Region 2 Pressure, 8e-4 sec.

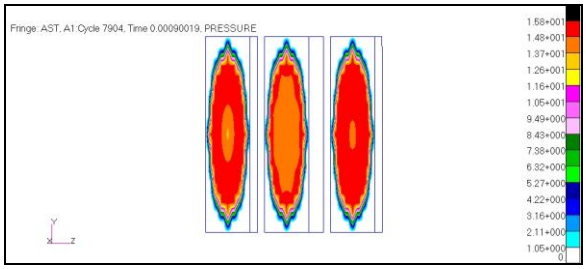

Figure 145: AST Euler Region 2 Pressure, 9.0e-4 sec.

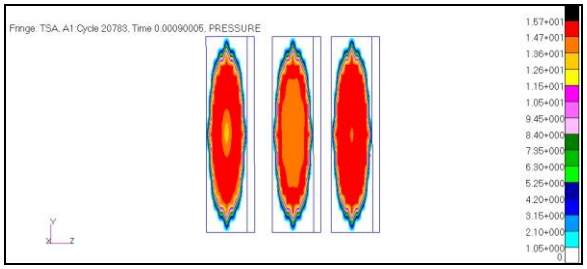

Figure 146: TSA Euler Region 2 Pressure, 9.0e-4 sec.

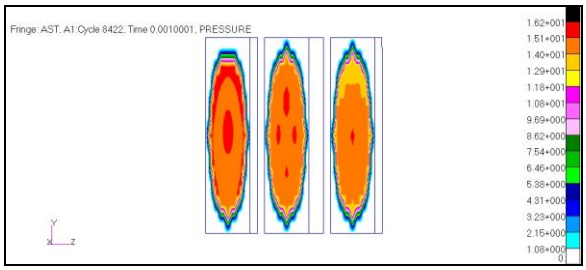

Figure 147: AST Euler Region 2 Pressure, 1.0e-3 sec.

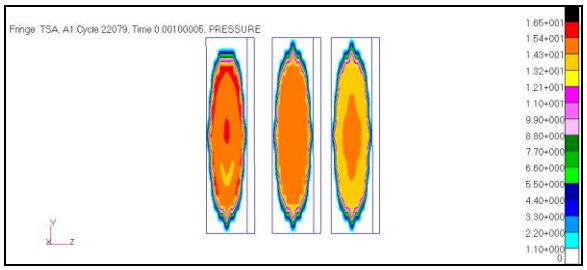

Figure 148: TSA Euler Region 2 Pressure, 1.0e-3 sec.

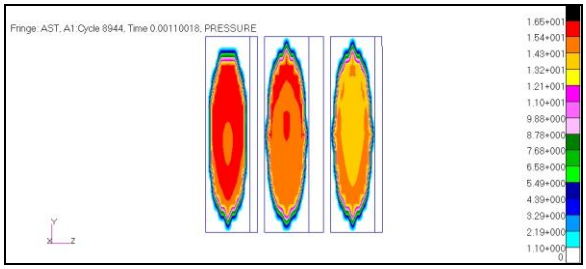

Figure 149: AST Euler Region 2 Pressure, 1.1e-3 sec.

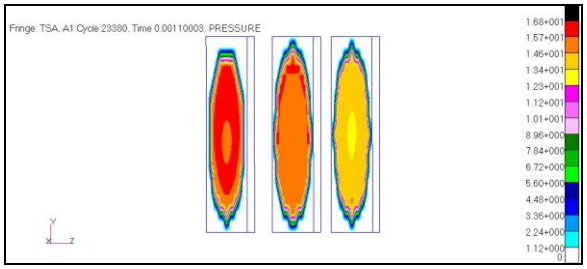

Figure 150: TSA Euler Region 2 Pressure, 1.1e-3 sec.

Conclusions

The main objective of this work was to calculate the over-pressure inside a target generated from a high velocity impact. This work shows that both penetrator configurations both produce a substantial over-pressure inside the target.

It was found that the AST penetrator transfers more kinetic energy to the target resulting in a higher over-pressure than the TSA penetrator. A factor in this is that a fragment of the aluminum from the TSA penetrator survives the initial impact and passes through the front plate into the interior of the target. For the AST penetrator there are no fragments which pass through the front plate, thus imparting all of its energy to the target upon impact. The deeper penetration of the TSA configuration might be favorable in some applications, if the mission profile calls for penetrating a hardened target without completely destroying the penetrator.

This simulation shows the distortional energy and internal energy peaks in the target to be higher in the TSA than in the AST. It also shows that though the AST produced a higher internal pressure in the target. The pressure rise occurred earlier for the TSA than it did for the AST.

References

1. "LOSAT Line-of-Sight Anti-Tank Weapons - High Mobility Multi-Purpose Wheeled Vehicle." *Army Technology*. Web. 26 Feb. 2011. <http://www.army-technology.com/projects/losat/>.
2. Organization, Lockheed Martin. "Compact Kinetic Energy Missile | Lockheed Martin." *Lockheed Martin*. Web. 26 Feb. 2011. <http://www.lockheedmartin.com/products/CompactKineticEnergyMissile/index.html>.
3. Zukas, Jonas A. *High Velocity Impact Dynamics*. New York: John Wiley & Sons, 1990. Print.
4. Huebner, Kenneth H., Donald L. Dewhirst, Douglas E. Smith, and Ted G. Byrom. *The Finite Element Method For Engineers*. Fourth ed. New York: John Wiley & Sons, 2001. Print.
5. Johnson, Gordon R., and William H. Cook. *A CONSTITUTIVE MODEL AND DATA FOR METALS SUBJECTED TO LARGE STRAINS, HIGH STRAIN RATES AND HIGH TEMPERATURES*. Rep. Print.
6. Meyers, Marc A., Lawrence Eugene. Murr, and Karl P. Staudhammer. *Shock-Wave and High-Strain-Rate Phenomena in Materials*. New York: Marcel Dekker, 1992. Print.

7. Blazynski, T. Z. *Materials at High Strain Rates.* New York: Elsevier Science, 1987. Print.
8. Zukas, Jonas A. *Introduction to Hydrocodes*. First ed. Amsterdam: Elsevier, 2004. Print.
9. MSC.Software Corporation. *Dytran 2008 r1 Theory Manual*
10. MSC.Software Corporation. *MD Nastran R3 Explicit Nonlinear (SOL 700) User's Guide*
11. Foster, W. A., Jr., "Final Report: Impact Energy Analysis," submitted to Dynetics, Inc., Huntsville, AL and U. S. Army Aviation and Missile Command AMSAM AC-RD-B Redstone Arsenal, AL, August 15, 2003. Print.
12. MSC.Software Corporation. *Dytran 2008 r1 Reference Manual*
13. Bower, Allan F. "Applied Mechanics of Solids (A.F. Bower) Chapter 2: Governing Eqs - 2.2Internal Forces." *Applied Mechanics of Solids (A.F. Bower) -- Home Page*. 2008. Web. 19 Apr. 2011. <http://solidmechanics.org/text/Chapter2_2/Chapter2_2.htm>.
14. Brand, Peter. "DISTORTIONAL ENERGY; INTERNAL ENERGY IN DYTRAN." *MSC SimCompanion*. 2 Oct. 2009. Web. <http://simcompanion.mscsoftware.com>.

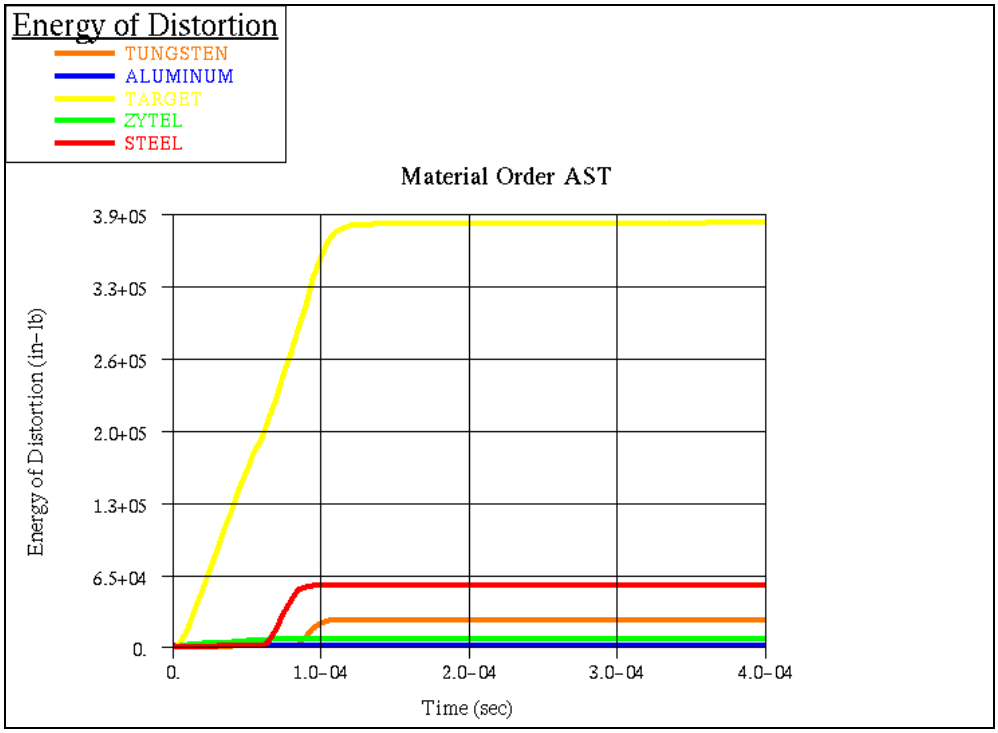

Figure 151: Foster - AST Energy of Distortion vs. Time [11]

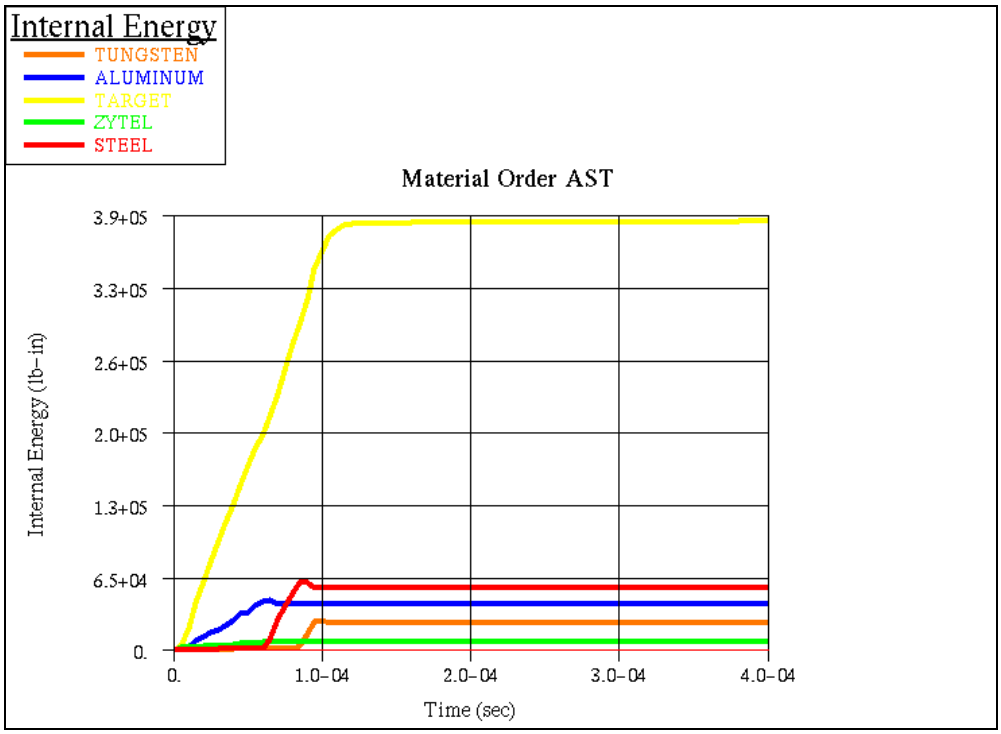

Figure 152: Foster - AST Internal Energy vs. Time [11]

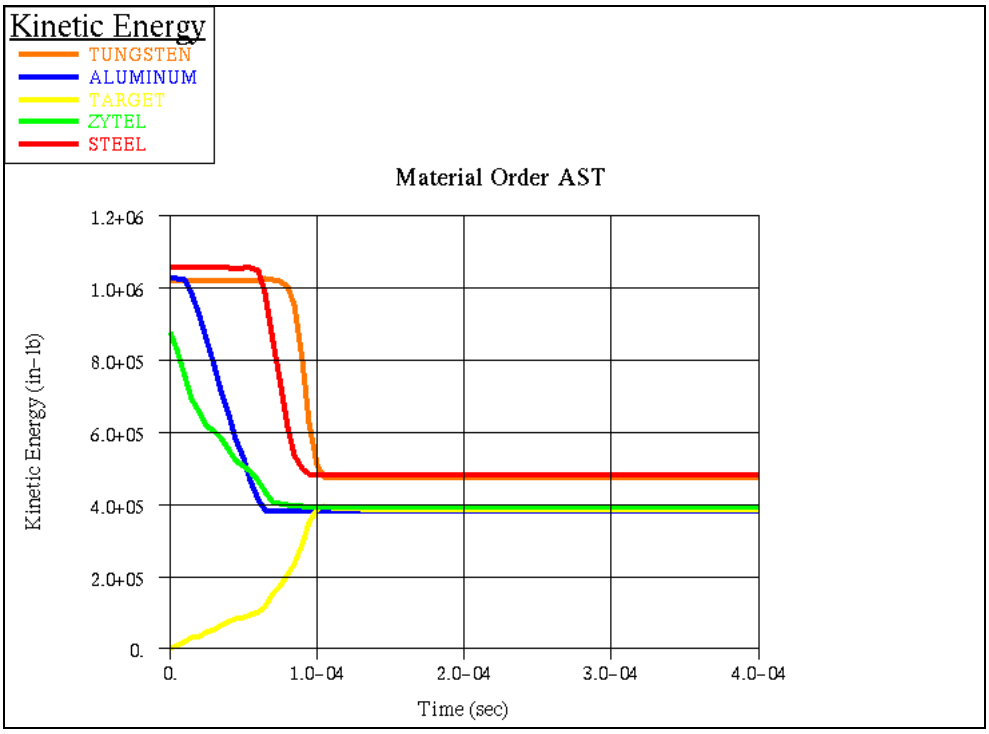

Figure 153: Foster - AST Kinetic Energy vs. Time [11]

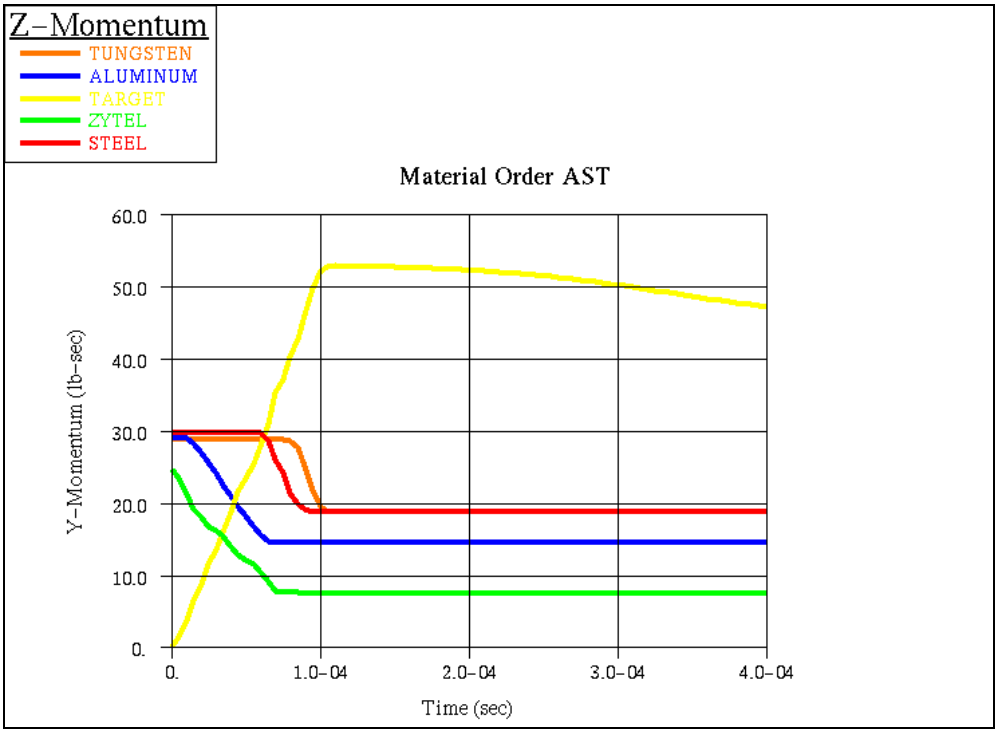

Figure 154: Foster - AST Z-Momentum vs. Time [11]

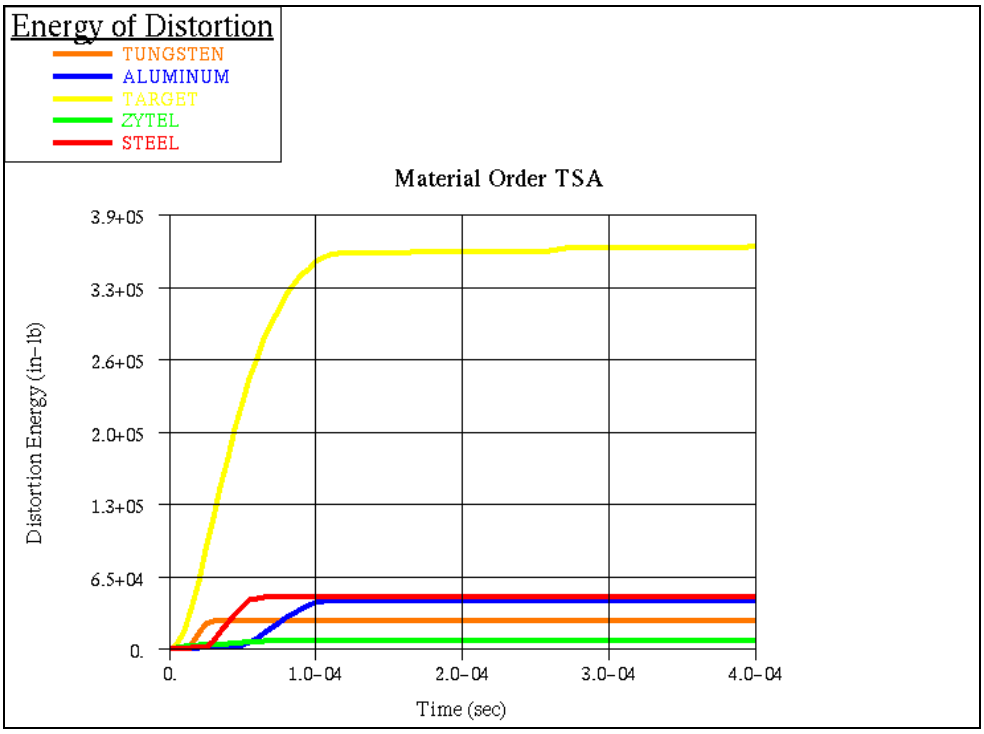

Figure 155: Foster - TSA Energy of Distortion vs. Time [11]

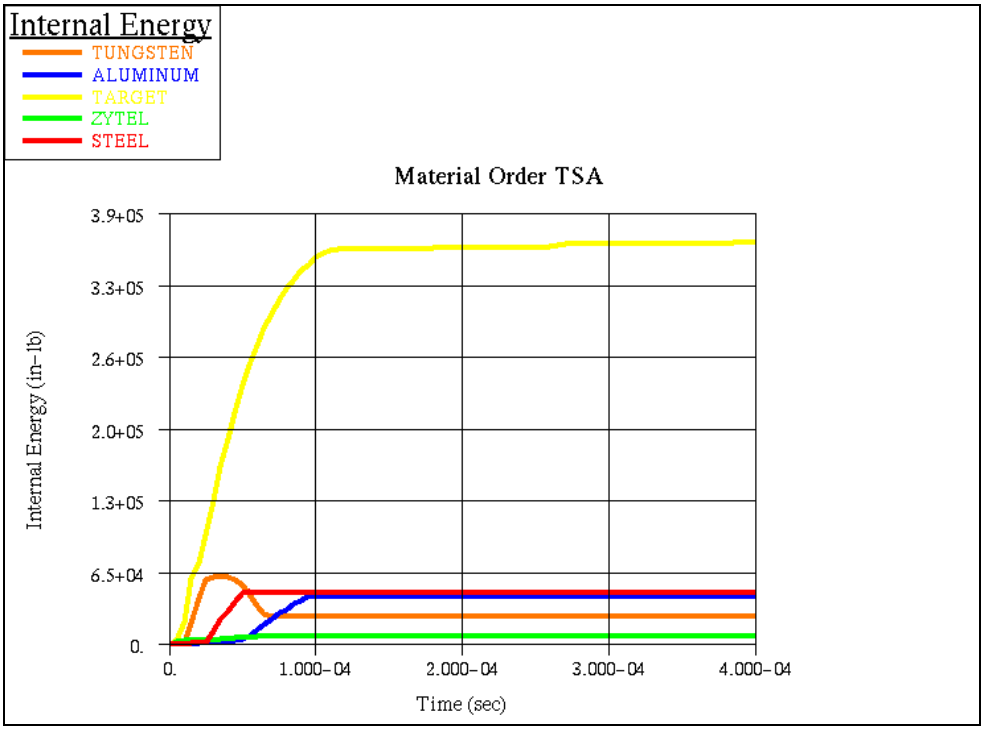

Figure 156: Foster - TSA Internal Energy vs. Time [11]

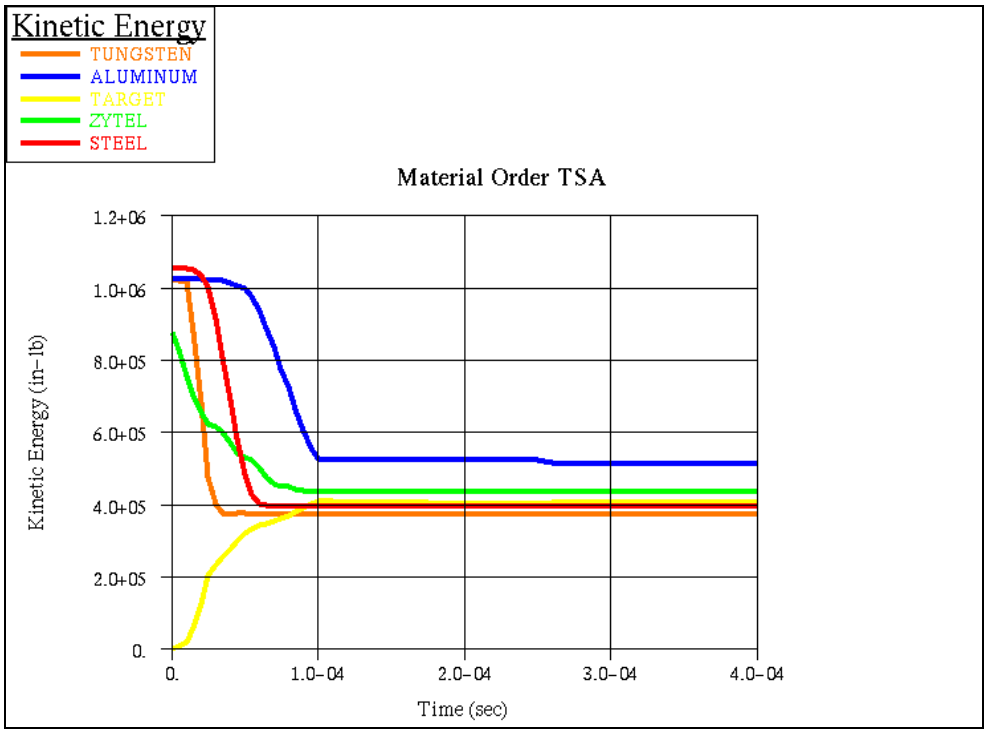

Figure 157: Foster TSA Kinetic Energy vs. Time [11]

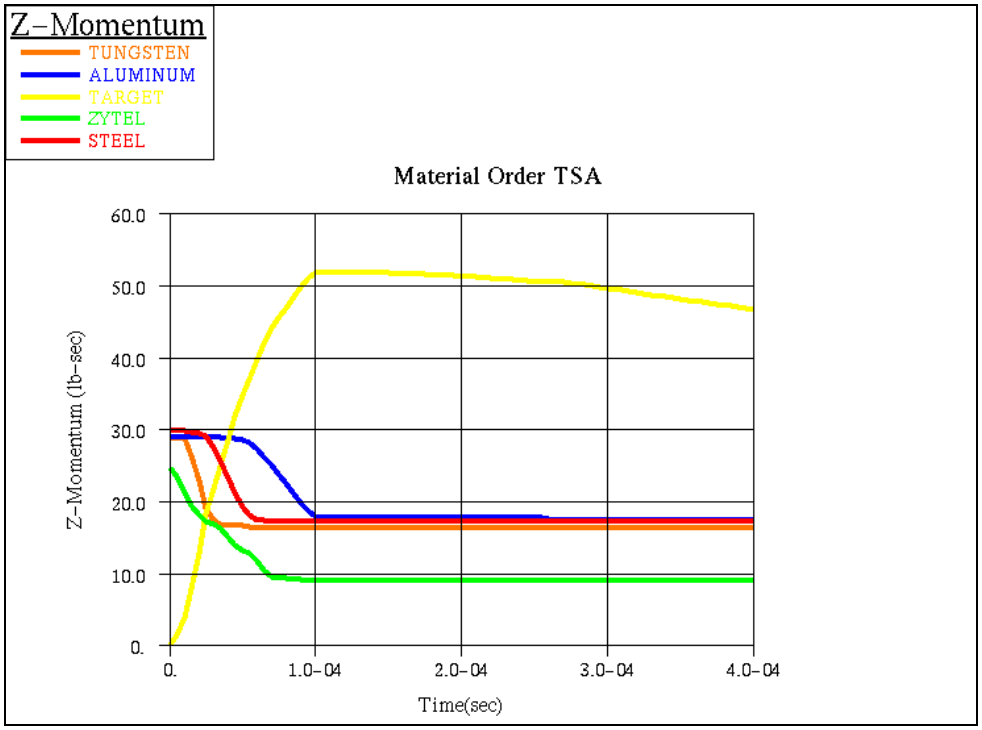

Figure 158: Foster TSA Kinetic Energy vs. Time [11]